J. Fluid Mech. (1997), *vol.* 343, *pp.* 43–72. Printed in the United Kingdom

© 1997 Cambridge University Press

Direct simulations of turbulent flow in a pipe rotating about its axis

By **P. ORLANDI** AND **M. FATICA**†
Università di Roma "La Sapienza" Dipartimento di Meccanica e Aeronautica,
via Eudossiana n^o 18 00184 Roma, Italy

(Received 24 March 1995 and in revised form 3 March 1997)

Flow in a circular pipe rotating about its axis, at low Reynolds number, is investigated. The simulation is performed by a finite difference scheme, second-order accurate in space and in time. A non-uniform grid in the radial direction yields accurate solutions with a reasonable number of grid points. The numerical method has been tested for the non-rotating pipe in the limit $\nu \to 0$ to prove the energy conservation properties. In the viscous case a grid refinement check has been performed and some conclusions about drag reduction have been reached. The mean and turbulent quantities have been compared with the numerical and experimental non-rotating pipe data of Eggels *et al.* (1994*a*, *b*). When the pipe rotates, a degree of drag reduction is achieved in the numerical simulations just as in the experiments. Through the visualization of the vorticity field the drag reduction has been related to the modification of the vortical structures near the wall. A comparison between the vorticity in the non-rotating and in the high rotation case has shown a spiral motion leading to the transport of streamwise vorticity far from the wall.

1. Introduction

The experimental study of turbulent circular pipe flow has attracted the interest of several scholars, owing to the simplicity of the experimental setup. The flow visualizations of Reynolds (1883), for example, can be considered a milestone for the understanding of turbulent and transitional flows. Later, Laufer (1954) performed measurements that, after many years, are still a good database of wall turbulence. The flow in a pipe has been recently used to test new measurement techniques such as PIV (particle image velocimetry) which permits the measurement of one component of the instantaneous vorticity field. On the other hand, the numerical simulation of turbulent pipe flow has received less interest than that in the plane channel because of the numerical difficulties in treating the singularity at the axis. Recently a direct simulation of turbulent pipe flow by finite differences has been performed by Eggels *et al.* (1994*b*, hereafter referred to as EUW), and their results have been compared with measurements performed by PIV and LDA (laser Doppler anemometry) and with direct simulations of a plane channel by Kim, Moin & Moser (1987, hereafter referred to as KMM) at the same Re_τ. During the revision process of the present paper further direct simulations of turbulent pipe flows have been performed by different numerical methods such as full spectral by Zhang *et al.* (1994) and by B-splines and spectral method by Loulou (1996).

---

† Present address: CTR, Stanford University, Stanford 94305, CA, USA.

LES (large eddy simulations) and direct numerical simulations in a rotating pipe by Eggels, Boersma & Nieuwstadt (1994*a*, hereafter referred to as EBN) were performed for moderate $N = V_{\theta 0}/U_b$. This non-dimensional rotation number relates the two relevant velocity scales in this flow: $V_{\theta 0}$, the velocity of the rotating wall, and $U_b = U_P/2$, the bulk velocity (U_P is the centreline streamwise velocity of the laminar Poiseuille flow). Just as in the experiments by Murakami & Kikuyama (1980) and Hirai, Takagi & Matsumoto (1988), drag reduction was observed in these later studies. The EBN simulation, however, did not consider high N where the experiments showed the re-laminarization of the flow. The present study is devoted to the study of the range of N not considered by EBN, that is the investigation of the flow field at high N ($N \leqslant 2$) but not so high as to include re-laminarization, and to the analysis of the modifications of the near-wall vortical structures, for a more satisfactory explanation of drag reduction. EBN uses the laboratory reference frame: then the wall of the pipe rotates with the velocity $V_{\theta 0}$. In the present simulations, on the other hand, a reference frame rotating with the wall has been chosen; thus the same boundary conditions as in the non-rotating case apply but the Coriolis body force appears.

The effects of solid-body rotation on turbulence in a circular pipe have similarities with three-dimensional boundary layers of practical importance, e.g. in swept wings of airplanes. Furthermore, the rotating pipe is a very good candidate to help in understanding swirling flows, which are important in applications connected with combustion and aeroacoustics. A further motivation for performing direct simulations at different values of the rotation number N is to provide a database useful for developing more efficient Reynolds-averaged models. Hirai *et al.* (1988), in fact, found that in the rotating pipe the standard k–ϵ turbulence model produces very poor results and that it is necessary to use full Reynolds stress models for better predictions. The database generated by the direct simulations permits the evaluation of the budget of each Reynolds stress, which is necessary to test and validate new closure models. The standard two-equation turbulence model did not give good predictions for the rotating pipe flow; however, it is interesting to investigate whether some of the new modifications introduced recently by Durbin (1991) and by Zeman (1995) are valid for rotating wall flows. For example Durbin (1991) related the eddy viscosity to the r.m.s. of the normal velocity rather than to the turbulent kinetic energy. Preliminary calculations with the present database have shown that in the non-rotating pipe the eddy viscosity relationship of Durbin (1991) gives the correct wall damping without introducing any *ad hoc* assumption. However when this model is applied to the rotating case, it does not account for the rotation effects in the outer region. The effects of the body force then could be modelled as suggested by Zeman (1995). Even though in this paper we do not describe the preliminary results that we obtained on the validity of these new ideas on the one-point closure models for wall-bounded rotating flows, we wish to point out that reliable Reynolds-averaged models are of urgent need for industries working in combustion and turbo-machinery. For this reason we are going to devote a future comprehensive study to this topic.

Since the near-wall vortical structures account for turbulence production as well as for wall friction, in this study flow visualizations in rotating and in non-rotating cases have been performed. These visualizations, together with profiles of high-order statistics (skewness and flatness) and two-point correlations, allowed us to understand, in a different way, the mechanism leading to drag reduction. The rotating pipe, in fact, is a very simple configuration where the solid-body rotation is oriented in the same direction as the streamwise vortices. From contour plots of the vorticity field it has been observed that the wall vortices are tilted in the direction of rotation and that their centre is displaced far from the wall. The consequent effect is to reduce the number and intensity of the ejection and sweep events. Joint p.d.f.s (probability density functions) of the velocity fluctuations confirmed this picture and permitted us to understand the formation of the turbulent stresses that are absent in non-rotating pipes.

2. Equations and numerical scheme

In the three-dimensional case, expressing the Navier–Stokes equations in primitive variables reduces the number of operations necessary to integrate the equations numerically. In cylindrical coordinates, when the variables $q_\theta = rv_\theta$, $q_r = rv_r$, $q_z = v_z$, are introduced, the continuity equation becomes

$$\frac{\partial q_r}{\partial r} + \frac{1}{r}\frac{\partial q_\theta}{\partial \theta} + r\frac{\partial q_z}{\partial z} = 0. \tag{2.1}$$

It is clear that the quantities q_i do not all have the same physical dimensions; this could be a matter of confusion. We wish to point out that these variables have been introduced for numerical reasons only. As discussed later, the introduction of q_r simplifies the treatment of the singularity at $r = 0$ and q_θ permits better accuracy near the axis.

The Navier–Stokes equations in terms of the new variables, in a reference frame rotating with the pipe wall, are

$$\begin{aligned} &\frac{\partial q_\theta}{\partial t} + \frac{\partial q_\theta/rq_r}{\partial r} + \frac{1}{r^2}\frac{\partial q_\theta^2}{\partial \theta} + \frac{\partial q_\theta q_z}{\partial z} + \frac{q_\theta}{r}\frac{q_r}{r} + Nq_r \\ &\quad = -\frac{\partial p}{\partial \theta} + \frac{1}{Re}\left[\frac{\partial}{\partial r} r\frac{\partial q_\theta/r}{\partial r} - \frac{q_\theta}{r^2} + \frac{1}{r^2}\frac{\partial^2 q_\theta}{\partial \theta^2} + \frac{\partial^2 q_\theta}{\partial z^2} + \frac{2}{r^2}\frac{\partial q_r}{\partial \theta}\right], \end{aligned} \tag{2.2a}$$

$$\begin{aligned} &\frac{\partial q_r}{\partial t} + \frac{\partial}{\partial r}\frac{q_r^2}{r} + \frac{\partial}{\partial \theta}\frac{q_\theta q_r}{r^2} + \frac{\partial q_r q_z}{\partial z} - \frac{q_\theta^2}{r^2} - Nq_\theta \\ &\quad = -r\frac{\partial p}{\partial r} + \frac{1}{Re}\left[\frac{\partial}{\partial r} r\frac{\partial q_r/r}{\partial r} - \frac{q_r}{r^2} + \frac{1}{r^2}\frac{\partial^2 q_r}{\partial \theta^2} + \frac{\partial^2 q_r}{\partial z^2} - \frac{2}{r^2}\frac{\partial q_\theta}{\partial \theta}\right], \end{aligned} \tag{2.2b}$$

$$\begin{aligned} &\frac{\partial q_z}{\partial t} + \frac{1}{r}\frac{\partial q_r q_z}{\partial r} + \frac{1}{r^2}\frac{\partial q_\theta q_z}{\partial \theta} + \frac{\partial q_z^2}{\partial z} \\ &\quad = -\frac{\partial p}{\partial z} - \overline{\frac{\partial P}{\partial z}} + \frac{1}{Re}\left[\frac{1}{r}\frac{\partial}{\partial r} r\frac{\partial q_z}{\partial r} + \frac{1}{r^2}\frac{\partial^2 q_z}{\partial \theta^2} + \frac{\partial^2 q_z}{\partial z^2}\right]. \end{aligned} \tag{2.2c}$$

The equations non-dimensionalized by the centreline streamwise velocity U_P of the laminar Poiseuille flow and by the pipe radius R give the dimensionless numbers $Re = U_P R/\nu$ and $N = 2\Omega R/U_P$. In this paper rather than the Rossby number $R_o = U_P/2\Omega R$ usually used in geophysical problems, the rotation number $N = 1/R_o$ has been adopted. This choice has been dictated by the fact that N has been previously used in studies of turbulent flows in rotating pipes. The mean pressure gradient in the q_z equation maintains the bulk velocity $U_b = \int q_z \mathrm{d}V$ constant; it is evaluated by integrating the discretized q_z equation. $\overline{\partial P/\partial z}$ is related to the mean wall friction velocity u_τ by $u_\tau = (|\overline{\partial P/\partial z}|/2)^{1/2}$.

In a finite difference scheme, the most compact form for the discrete div and grad operators is achieved by locating the velocity components at the centre of the faces and the pressure at the centre of the cell. The numerical scheme was described in the paper by Verzicco & Orlandi (1996), where it was validated by two-dimensional, axisymmetric and three-dimensional flows. The check of the accurate treatment of the singularity was done by letting a dipole move across the axis where large variations of radial velocity occur. The simulation showed that the dipolar structure maintains its shape and that in the inviscid case the energy was conserved.

Here we summarize the main features of the method. Viscous and advective terms are discretized by centred second-order schemes. In the three-dimensional case, in the limit of $\nu \to 0$, energy is conserved by the discretized equations. The system of equations was solved by a fractional step method (Rai & Moin 1991). In a first step a non-solenoidal velocity field $\hat{q}_i$ is computed, and, if the pressure gradients at the previous time step are retained, the boundary conditions for $\hat{q}_i$ are simplified. A scalar quantity Φ is introduced to project the non-solenoidal field onto a solenoidal one. The large band matrix associated with the elliptic equation for Φ is reduced to a tridiagonal matrix by periodic fast Fourier transforms in the azimuthal and in the axial directions. This procedure is very efficient for obtaining the solenoidal velocity within round-off errors. The amount of CPU time required to evaluate Φ is less than the amount of CPU time necessary to solve for the non-solenoidal field. The updated pressure is computed from the scalar Φ. A third order Runge–Kutta scheme, described by Rai & Moin (1991), was used to advance in time through three sub-steps. The viscous terms are treated implicitly by the Crank–Nicolson scheme.

In cylindrical coordinates, as mentioned before, the equations for the velocity components are singular at $r = 0$. If staggered 'fluxes' are used, one can set $q_r = 0$ at the centreline, and the q_r equation can be discretized at the points $i + \frac{1}{2}, 2, k + \frac{1}{2}$ without any approximation. The viscous terms in the radial direction at the first point close to the wall for the q_θ and q_z equations have been approximated as in Rai & Moin (1991) for the plane channel. The discretization of the q_z and q_θ equations at the first grid position near the axis does not require any approximation for the radial derivatives.

Periodicity has been imposed in the streamwise direction in a domain with length L_Z/R depending on the rotation number N. Finite differences have the advantage of permitting the application of arbitrary coordinate transformations to cluster grid points in regions of high gradients. An analytical transformation by the hyperbolic tangent method permits the first grid point to be at a distance $y^+ < 1$ from the wall. This clustering is necessary to fully resolve the thin vortical layers near the wall responsible for the wall friction and for the turbulence production. Although the Reynolds number is low, the grid spacing in the central region of the pipe is not small enough to consider the flow fully resolved. However the present simulations have radial grid spacing close to that used in the full channel by KMM. Moreover it is clear that the resolution for the circular pipe is better than in the plane channel, since the polar coordinates reduce the size $(r\Delta\theta)$ of the physical grid near the axis. The check of the numerical model is given in the Appendix, where also some physical conclusions are drawn from the coarse simulations.

3. Results

When the wall of a pipe rotates there is some similarity with a three-dimensional boundary layer, a flow with more practical applications. For the latter flow it is difficult to design an experiment with boundary conditions perfectly reproducible in a direct numerical simulation. On the other hand experiments on rotating pipes can be easily realized and numerical simulations can be performed with one to one correspondence between the geometrical conditions in the experiment. The detailed knowledge of this simple flow through experimental and numerical studies could help to understand the effects of the modifications of the flow structures in more practical problems such as the flow on swept wings. To see better the analogy between these two flows the rotating pipe flow, in a reference frame rotating with the wall, can be thought of as a flow where the Coriolis force acts as a local azimuthal pressure gradient that affects the orientation, the spacing and the size of the streamwise vortices. Sendstad & Moin (1992), by a direct simulation of a three-dimensional plane channel, observed drag reduction and explained this phenomenon by the tilting of the streamwise vortices by the mean spanwise pressure gradient. In the rotating pipe experiments by Kikuyama, Murakami & Nishibon (1983*a*), Kikuyama *et al.* (1983*b*) and Reich & Beer (1989), drag as well as turbulence reduction was measured as the rotation rate was increased. At very high rotation speeds a sort of laminarization was also observed. This condition is characterized by an averaged $\langle v_z \rangle$ similar to the laminar Poiseuille profile. In the experiments, time averages of the signals taken at a single point were reported. On the other hand, in direct numerical simulations the averaging is done in time and space as is described in the Appendix. The changes in the mean and turbulent quantities in the experiments by Nishibori, Kikuyama & Murakami (1987) and by Reich & Beer (1989) were explained by a general connection with the effects of the centrifugal force, without mentioning any connection to the modifications of the near-wall vortical structures. Our belief is that changes in turbulent wall flows strongly depend on the modifications of the near wall vortical structures. Thus, as in the case of Sendstadt & Moin (1992), we are using numerical direct simulations of rotating pipes to visualize the near-wall vorticity field and to connect the changes in the profiles of turbulent quantities to these visualizations.

To our knowledge the present study and that by EBN are the only direct simulation studies at present available. EBN performed direct and large-eddy simulations at low rotation rates, $N = 0.31$ and $N = 0.62$, and presented the profiles of second-order turbulence statistics without investigating the modifications of the vortical structures in the wall region. In the present study simulations have been performed in the same range of N considered by Reich & Beer (1989) and Hirai *et al.* (1988). The simulations were performed at a Reynolds number (Re) close to the smallest Re in the experiment by Reich & Beer (1989). The Reynolds number is defined as $Re = U_P R/\nu = U_b D/\nu = 4900$; the bulk velocity is $U_b = 0.50 U_P$, where U_P is the maximum value of the Poiseuille profile.

Choosing the length of the computational box for direct simulations of wall turbulent flows is an important issue. EUW used axial two-point correlations of the r.m.s. velocity components to show that for $N = 0$ a length of the pipe $L_Z = 10R$ is sufficient to allow these correlations to drop to zero. In contrast, when the pipe rotates, flow visualizations by Nishibori *et al.* (1987), at high rotation ($N \approx 2$), showed that in the central part of the pipe elongated coherent structures form and that, at even higher rotation rates, the variations in the streamwise direction disappear, in agreement with the Taylor–Proudman theorem. These flow visualizations forced us to verify whether the $L_z = 10R$ length is sufficient when the pipe is rotating. The check was done at $N = 2$, the highest N in this study, and it was observed that with $L_z/R = 10$ the turbulent stresses $\langle v_z' v_r' \rangle$ and $\langle v_r' v_\theta' \rangle$ did not converge to the statistical steady state after 200 time units. On the other hand, when the length was increased to $L_z/R = 15$ and to $L_z/R = 20$, by keeping the same Δz a convergence to the statistical steady state was reached. Furthermore it has been observed that the elongated structures in the central region of the pipe have long time scales, requiring a longer time to reach statistical steady state than in the non-rotating case. Although

N	H(OF)	H(MK)	U_{CL}(OF)	U_{CL}(RB)	λ/λ_0(OF)	λ/λ_0(RB)	λ/λ_0(KM)
0	1.637	1.625	1.306	1.270	1.00	1.	1.
0.5	1.747	1.687	1.440	1.350	0.8386	0.9230	0.8523
1.0	1.771	1.812	1.503	1.457	0.8290	0.7692	0.7035
2.0	1.913	1.969	1.660	1.689	0.8247	0.6670	0.5898

TABLE 1. Table of the values of the global quantities in the present simulation indicated by (OF) at $Re = 5000$, and in the experiments by Reich & Beer (1989) (RB) at $Re = 5000$, by Murakami & Kikuyama (1987) (MK) at $Re = 10000$ and by Kikuyama *et al.* (1983*b*) (KM) at $Re = 7500$.

at $N < 2$ a length $L_z/R = 10$ is sufficient, the simulations were performed with the same length used for $N = 2$ ($L_z/R = 15$).

Before investigating the radial profiles of the mean and turbulent quantities, a comparison between some of the global quantities in the present simulations and in the experiments is shown in table 1. The results by Reich & Beer (1989) are at $Re = 5000$ close to the present one, while the results by Nishibori *et al.* (1987) were at $Re = 10000$ and those by Kikuyama *et al.* (1983*b*) at $Re = 7500$ and at $L_z/D = 120$. The shape factor H, if we introduce $V_z = \langle v_z \rangle / U_{CL}$, is defined as $H = \int (1 - V_z)\mathrm{d}r / \int V_z(1 - V_z)\mathrm{d}r$ with $U_{CL} = \langle v_z \rangle_{CL}$. In table 1 H and U_{CL}/U_b from the direct simulation agree satisfactorily well with the experiments. However, the wall friction ($\lambda = 8(u_\tau/U_b)^2$) reduction in the present simulations is lower than that in the experiments, showing a negligible dependence on N for $N > 0.5$. The low Re of the simulations could be a cause of this difference since the experiments by Kikuyama *et al.* (1983*b*) show a reduced dependence of the friction coefficients when the Reynolds number decreases. However, the Reich & Beer (1989) experiment was at the same Reynolds number; thus, a further reason for the difference could be the influence of the entrance conditions on the measurements. This is a more plausible reason because Murakami & Kikuyama (1980) showed that the loss coefficient depends on the axial location of the measurements. Perhaps $L_z/D = 120$, the location where Reich & Beer took the measurements, is still not sufficient to achieve the condition of fully developed rotating pipe flow. In addition it should be taken into account that the direct simulations are performed at constant mass flow rate ($U_b = 0.5$); in the experiment, on the other hand, usually the head of the pump is kept constant. Thus the flow conditions are different, and this could produce effects on the friction coefficients. Clearly this should be tested by a comparison between simulations at constant mass flow rate and at constant u_τ. This will be done in the near future in a more applied study, devoted also to study the real energy saving in rotating pipes. The present study, devoted to the physics of the near-wall turbulence, focuses on the important issue of predicting and explaining drag reduction in rotating pipes. We have carefully checked that the results do not depend on the length of the computational domain in z and on the grid resolution. As a further comment we believe that if the numerics had an effect on λ, it should be largest at $N = 0$, when the spatial gradients of the velocity field are greater than for $N > 0$. In contrast, at $N = 0$ the simulation predicts $\lambda = 0.0385$ in good agreement with the theoretical value $\lambda = 0.0378$, evaluated by the relationship $\lambda = 0.3164 Re^{-0.25}$.

In figure 1 the mean velocity profiles in wall units show the drag reduction through the upward shifting of the log law. As usual y^+ indicates the distance from the wall in wall units. In the pipe it is defined as $y^+ = (1 - r)u_\tau/\nu$. The tendency towards laminarization is better shown by the profiles scaled with the bulk velocity.

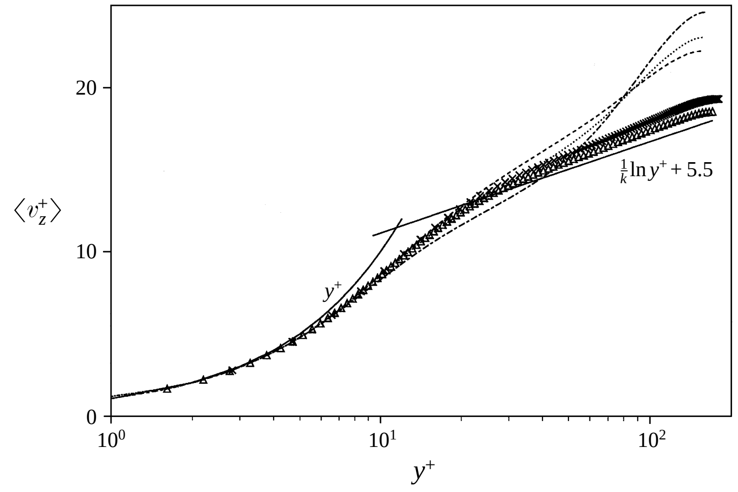

FIGURE 1. Averaged streamwise velocity profiles in wall units for - - - - , $N = 0.5$; ········ , $N = 1.0$; —-— , $N = 2.0$; △ , $N = 0$; × , EUW.

Figure 2 shows that the axial velocity profiles approach the Poiseuille profile when N increases, in agreement with the experimental observations that at $N = 3$ an almost parabolic profile was achieved. While for $N < 1$ the size of the buffer region remains unchanged, at $N = 2$ the buffer region almost completely disappears, and a first log region appears just after the viscous region, corresponding to the region where the turbulent energy is constant. Figure 2 shows that the axial velocity profiles, scaled with the bulk velocity, have at $y_d \approx 0.40$ almost the same value $\langle v_z \rangle / U_b = 1.14$. A similar behaviour was observed in the experiments by Reich & Beer (1989) and in the simulation by EBN. The present y_d agrees with the value $y_d = 0.37$ found by Kikuyama *et al.* (1983*a*) and differs from $y_d = 0.33$ and $y_d = 0.3$ found respectively by Reich & Beer (1989) and by EBN. Figure 2 shows that the variation with N of our profiles is in qualitative agreement with those measured by Reich & Beer (1989). A better agreement is obtained by scaling the experimental profiles at $N > 0$ with the ratio between the centreline velocity of the experiment and of the simulation at $N = 0$. Since the Reynolds number is the same the reason for the difference between the profiles, at $N = 0$, of the numerical simulation and of Reich & Beer (1989) should be the effect of the entrance conditions in the experiment.

A mathematical explanation of the occurrence of the fixed point in figure 2 was not found, but it was observed that close to the location where the profiles of $\langle v_z \rangle$ collapse there is a point with $\langle \omega_z \rangle = 0$. Figure 3 shows that in the profile of $\langle \omega_z \rangle$ there are two zero points, and they depend on the mean profile of $r\langle v_\theta \rangle$ (figure 4*a*). EBN proved, from the equation of $\langle v_\theta \rangle$, that near the wall the tangential velocity must be proportional to r and that in the inner field it is proportional to r^2. The first crossing, close to $y = 0$, occurs where $\langle v_\theta \rangle$ passes from a linear to a parabolic profile. The second crossing, from the vorticity definition, coincides with the minimum of $r\langle v_\theta \rangle$ as shown in figure 4(*a*). When $\langle v_\theta \rangle$ is scaled with the wall rotational velocity $V_{\theta 0}$, Reich & Beer (1989) claimed that it is independent of N and of Re. The same outcome was found by Kikuyama *et al.* (1983*a*, *b*) in their numerous experiments. In our simulations, performed in the rotating frame, to have the same scaling as in the experiment the linear solid-body rotation velocity Ωr must be added to $\langle v_\theta \rangle$. Moreover, the dimensional $\langle v_\theta \rangle$ should be scaled with the centreline velocity. By this operation

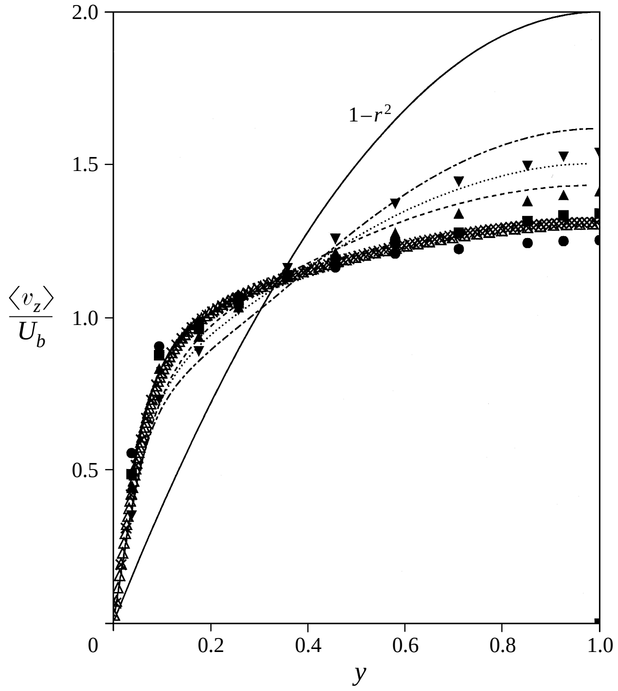

FIGURE 2. Averaged streamwise velocity profiles scaled with the bulk velocity U_b: ---- , $N = 0.5$; ······· , $N = 1.0$; —-— , $N = 2.0$; △ , $N = 0$; × , EUW. Closed symbols are from experiments by Reich & Beer (1989) at $Re = 5000$: ● , $N = 0$; ■ , $N = 0.5$; ▲, $N = 1$; ▼, $N = 2$.

the profiles of $\langle w_\theta \rangle = \langle v_\theta \rangle U_{CL} 2/N + r$ in figure 4(*b*) show a slight dependence on N. In figure 4(*b*) the values by Kikuyama *et al.* (1983*b*) at $Re = 10000$ reported in the paper by Hirai *et al.* (1988) are included. We took the data from Hirai *et al.*'s paper because these were given at each N separately. In the original paper by Kikuyama *et al.* (1983*b*) it was difficult to read the data, and those at $N = 0.5$ were given only for a few radial locations. A very careful observation of the data at $N = 0.5$, however, shows that the symbols do not exactly coincide with those at $N = 1$. The values of Reich & Beer (1989) were not included since these coincided exactly with the theoretical curve $\langle w_\theta \rangle / V_{\theta 0} = r^2$. The present $\langle w_\theta \rangle$ profiles do not collapse on a single curve, as in Reich & Beer (1989); however, they are in a good agreement with the Kikuyama *et al.* data. Also in the direct simulation at two close values of N EBN found an imperfect collapse of the profiles. On the other hand, the EBN profiles collapsed in the higher Reynolds number LES simulations at $N = 0.71$. From these considerations, we could conjecture that the discrepancies with the experimental results of Reich & Beer (1989) could be due, once more, to the effects of the entrance condition and not to *Re*, since in the experiments independence of *Re* was found. We checked that the lack of similarity in figure 4(*b*) did not depend on the insufficient time integration to reach the steady state. Moreover, the averages were done with fields with $Q_\theta = \int q_\theta \mathrm{d}V$ constant. The independence of the radial resolution was also investigated: simulations with 49 and 97 points in the radial directions produced the same $\langle w_\theta \rangle$ profiles. The check that our $\langle v_\theta \rangle$ at the steady state satisfies the relationship

$$\langle v'_\theta v'_r \rangle - \frac{1}{Re} r \frac{\partial \langle v_\theta \rangle / r}{\partial r} = 0 \qquad (3.1)$$

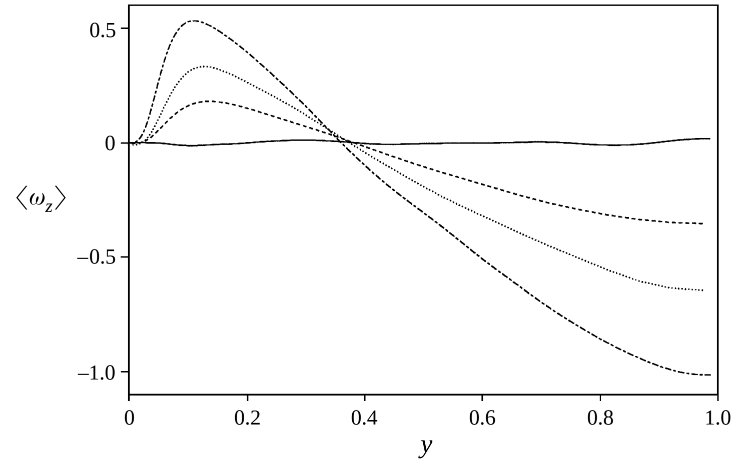

FIGURE 3. Mean streamwise vorticity profiles: ——— , $N = 0$; - - - - , $N = 0.5$; ········ , $N = 1.0$; — - — , $N = 2.0$.

was done, confirming the assertion in EBN that near the wall the $\langle v_\theta \rangle$ profile must go to zero with a zero slope. Equation (3.1) shows that if the theoretical relationship $\langle w_\theta \rangle / V_{\theta 0} = r^2$ holds even close to the wall, $\langle v'_\theta v'_r \rangle$ is different from zero at the wall. The Kikuyama *et al.* (1983*b*) measurements at $N = 0.5$ show for $y < 0.2$ a tendency towards a linear profile, even if the measurement point closest to the wall is on the theoretical curve. Our belief is that measurements near the wall are difficult when the wall rotates, as is confirmed by some inconsistency of the data which does not appear in the central region. Inside the channel at $N = 0.5$, our data and that of Kikuyama *et al.* (1983*b*) do not coincide with the theoretical curve. By increasing N our results smoothly approach the theoretical curve while the Kikuyama *et al.* data at $N = 1$ and $N = 2$ lie on the theoretical curve. The smooth increase of $\langle w_\theta \rangle / V_{\theta 0}$ with N of the numerical simulation can be explained as a viscous correction that is greater for smaller N.

The influence of the rotation on the second-order turbulence statistics was investigated by EBN. They found that the largest effects occur on the streamwise r.m.s. velocity; this should be expected, since the rotation affects the production of turbulent energy, which near the wall is mainly due to $\langle v'_z v'_z \rangle$. Moreover according to the Taylor–Proudman theorem, a rotating flow tends to reduce the gradients in the direction of the rotation vector. This reduction, however, is not as strong as in homogeneous flows because of the turbulence production near the wall. The r.m.s. velocity profiles, scaled by the centreline velocity, in figure 5(*a*–*c*) show a greater reduction of the streamwise r.m.s. than of the other two components. Figure 5(*a*) shows that for $N \leqslant 1$ the peak of $\langle v'^2_z \rangle^{1/2}$ is reduced but an increase in the central part of the pipe is observed. On the other hand for $N = 2$ a flat region is achieved with a value comparable to that of $\langle v'^2_\theta \rangle^{1/2}$. In the experiment by Nishibori *et al.* (1987) the measurements of v'_z at $N \geqslant 0$ showed strong dependence on the distance from the inlet section; however, although not showing any flattening the reduction of the wall peak was observed. In the experiment, the authors presented profiles at $Re = 3 \times 10^4$ at three streamwise locations, and the reduction with N of the r.m.s. component in the last station agrees with our results. Since direct simulations at higher Re are not affordable, we conjecture that this flattening is a low-Reynolds-number effect. This is realistic, since even in the KMM simulations, a strong interaction between the

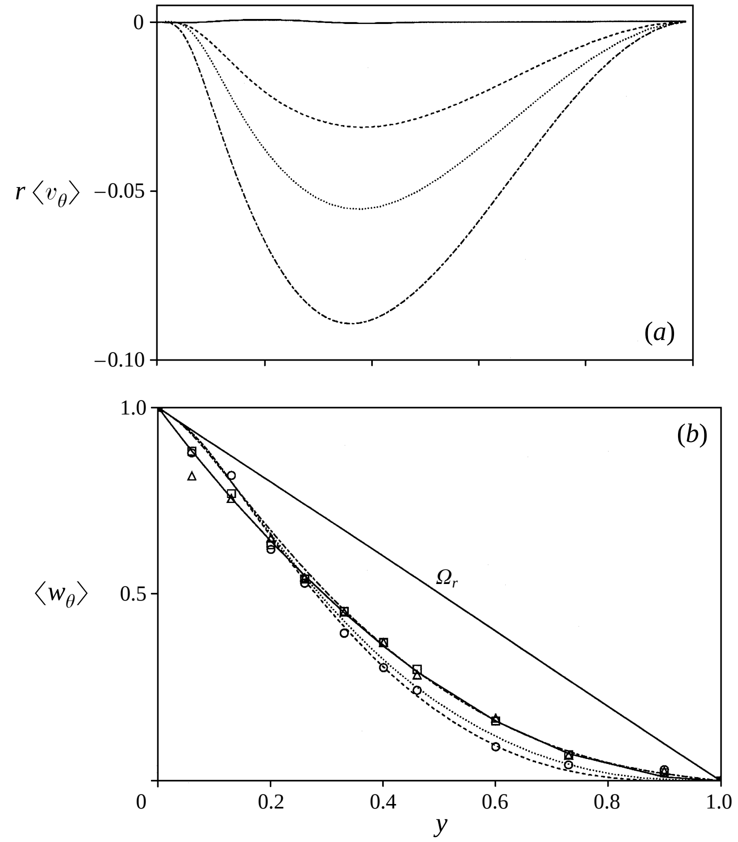

FIGURE 4. Radial profiles of (*a*) swirl and (*b*) radial velocity in the laboratory reference frame - - - - , $N = 0.5$; ········ , $N = 1.0$; — - — , $N = 2.0$; ——— , theoretical r^2; ○ , $N = 0.5$; △ , $N = 1$, □ , $N = 2$ (symbols experiment by Kikuyama *et al.* 1983*b*).

wall and the centre of the channel occurs. In the present case, as is shown later, the near-wall vortical structures increase their size as N increases and thus the turbulence level increases far from the wall. In the Appendix it is shown that this flattening does not depend on the resolution or on the length of the pipe.

As found by EBN, the $\langle v_\theta'^2 \rangle^{1/2}$ peak does not change appreciably with N. They found that going from $N = 0$ to $N = 0.32$ the peak increases weakly in the direct simulation at $Re_\tau = 180$ and decreases in the LES at $Re_\tau = 1050$. Our simulation shows an irrelevant decrease for $N < 1$, an increase for $N = 1$, and for $N = 2$ values close to those for $N = 1$ with a tendency to produce, as for v_z' r.m.s., profiles with a flat region in a large portion of the pipe. Although there are differences between the present and the EBN simulations, both show that near the wall the rotation has less influence on $\langle v_\theta'^2 \rangle$ than on $\langle v_z'^2 \rangle$. The peak of the radial velocity r.m.s. decreases near the wall for $N < 1$, as shown by the LES in EBN; for $N \geqslant 1$ the peak is translated towards the centre of the pipe. We could not find other results in the literature that show this effect at high rotation. The overall picture derived from figure 5(*a–c*) is that there is a tendency towards isotropy of the three velocity fluctuations.

In the non-rotating pipe $\langle v_r' v_z' \rangle$ is the only stress; it is reduced when the pipe rotates, as measured by Kikuyama *et al.* (1983*a*, *b*). Figure 5(*d*) shows that near the wall this stress, in wall units, for $N \leqslant 1$ decreases with N and then increases for $N = 2$. At

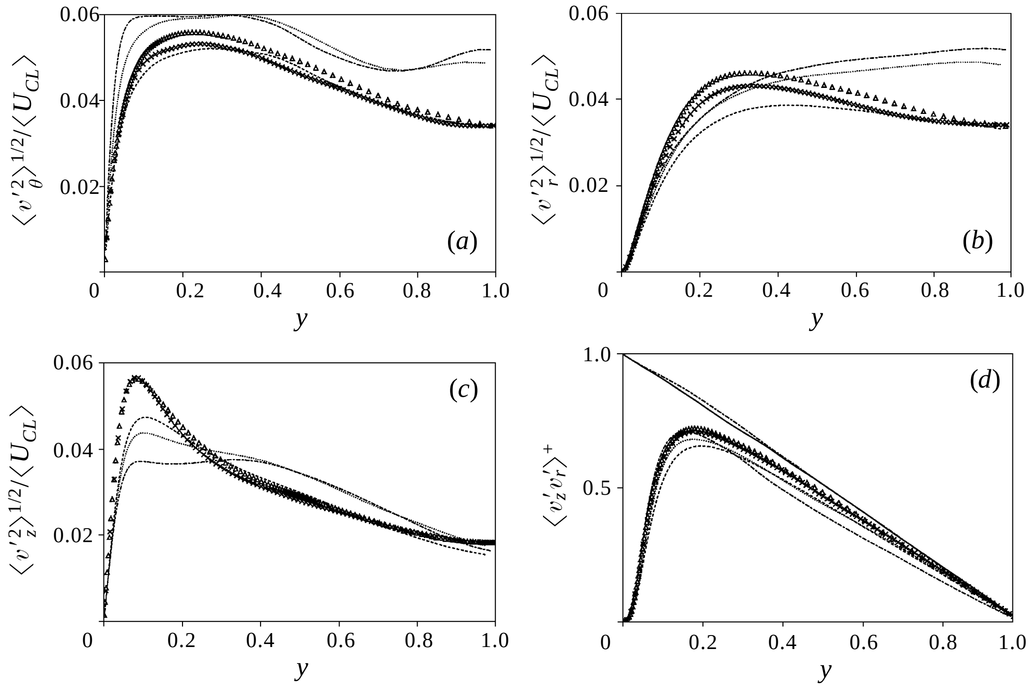

FIGURE 5. RMS profiles of (*a*) azimuthal, (*b*) radial and (*c*) axial velocity components; (*d*) $\langle v'_z v'_r \rangle$ Reynolds stress in wall units, total stress: ——— , $N = 0$; —·— , $N = 2$; ---- , $N = 0.5$; ········ , $N = 1.0$; — — — , $N = 2.0$; △ , $N = 0$; × , EUW.

$N = 2$, on the other hand, $\langle v'_r v'_z \rangle^+$ decreases in the central region in accordance with the increase of the viscous stress. In figure 5(*d*) the total stress, that is the sum of the viscous and the turbulent stress, is given for the two extreme cases $N = 0$ and $N = 2$. The linear profile in the non-rotating case was obtained by averaging 25 fields separated from each other by 2 time units. At $N = 2$, as shown in the experiments and in the present simulations, elongated structures form in the central region of the pipe. These structures are associated with long-time scales that induce slow variations in the Reynolds stress that require more time to reach the statistical steady state. Near the wall, at $N = 2$, the convergence of the turbulent stresses to the steady state is comparable to that at $N = 0$. In fact, in the rotating and in the non-rotating cases the eddies in this region have short time scales. Because of the slow motion of the large helical scales at $N = 2$ the statistics were evaluated with 65 fields. The simulations, moreover, have shown that the statistical steady state is achieved only when L_z/R is long enough to capture the full length of the large scales in the central region.

When the pipe rotates the other two Reynolds stress become comparable to $\langle v'_r v'_z \rangle$ with high values of $\langle v'_\theta v'_z \rangle$ close to the rotating wall as figure 6(*a*) shows. Figure 6(*a*) also shows that for $0 < N < 1$ the largest variations occur near the wall, while, on the other hand, the level is negligible in the central part for low N and becomes appreciable at high N. The radial oscillations of $\langle v'_z v'_\theta \rangle$ at high N are due to the large-scale structures in the central part of the pipe, which contribute to $\langle \omega_z \rangle$ (figure 3). When the rotation decreases, the strength of these large scales is weaker and the magnitude of $\langle v'_z v'_\theta \rangle$ is negligible. The intense peak of $\langle v'_z v'_\theta \rangle$ near the wall is related to the tilting of the near-wall vortical structures that increases the amount of correlation between v'_z and v'_θ, as is shown below by the joint p.d.f. Figure 6(*b*) shows that the

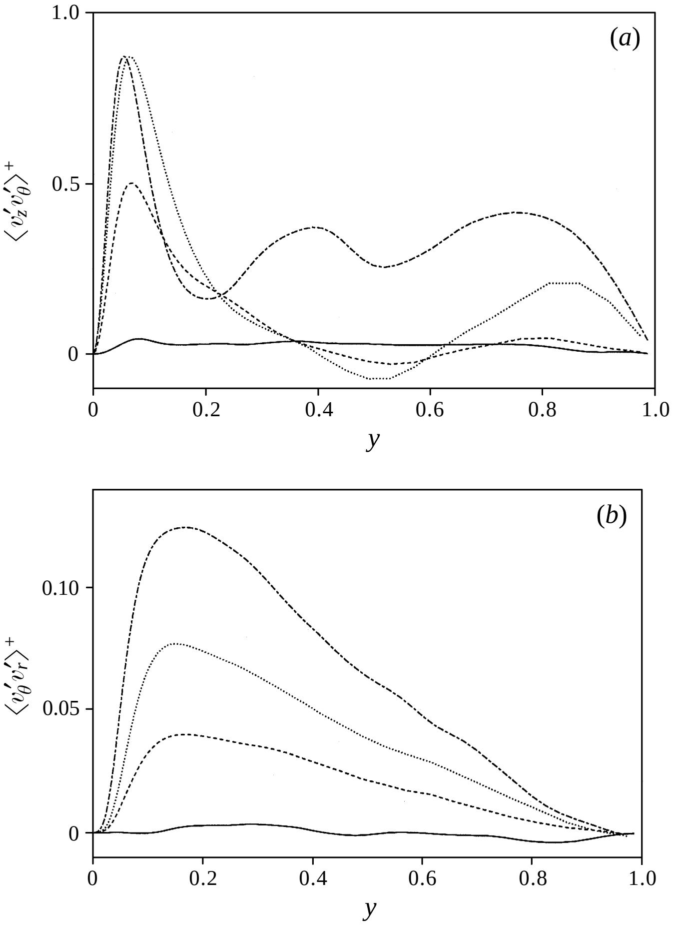

FIGURE 6. Profiles of Reynolds stresses: ——— , $N = 0$; - - - - , $N = 0.5$; ········ , $N = 1.0$; — - — , $N = 2.0$.

profiles of $\langle v_\theta' v_r' \rangle$ are approximately linear in the central region of the pipe and, as previously mentioned, this agrees with the parabolic profile of $\langle v_\theta \rangle$. However the slope is not proportional to N to give the perfect collapse of all the curves in figure 4(*b*). This lack of proportionality with N was found for other quantities: in fact Kikuyama *et al.* (1983*b*) reported the maximum centreline velocity as a function of N showing that between $N = 1$ and $N = 3$ it grows linearly, while at $N = 0.5$ it deviates from the linear slope. If the theoretical profile $\langle w_\theta \rangle = r^2$ were to hold up to the wall, $\langle v_\theta' v_r' \rangle$ should be linear and have a value there different from zero. This is of course not possible; therefore, close to the wall the stress $\langle v_\theta' v_r' \rangle$ decrease and consequently $\langle w_\theta \rangle$, as shown in figure 4(*b*), differs from the theoretical curve. At $y = 0.05$ the $\langle v_\theta' v_r' \rangle$ stresses scale with N and this linear scaling explains why in Figure 4(*b*) near the wall the $\langle w_\theta \rangle$ profiles collapse onto a single curve.

In three-dimensional boundary layers Schwarz & Bradshaw (1994) evaluated the structure parameter $a_1 = [\langle u'v' \rangle^2 + \langle v'w' \rangle^2]^{1/2} / \overline{q^2}$ to characterize the flow. This quantity can be regarded as the efficiency of the eddies in producing turbulent shear stresses for a given amount of turbulence energy. Experimentally, they found that for $y/\delta_{99} < 0.2$, a_1 decreases moderately with the increase of cross-flow, while in the outer half of the

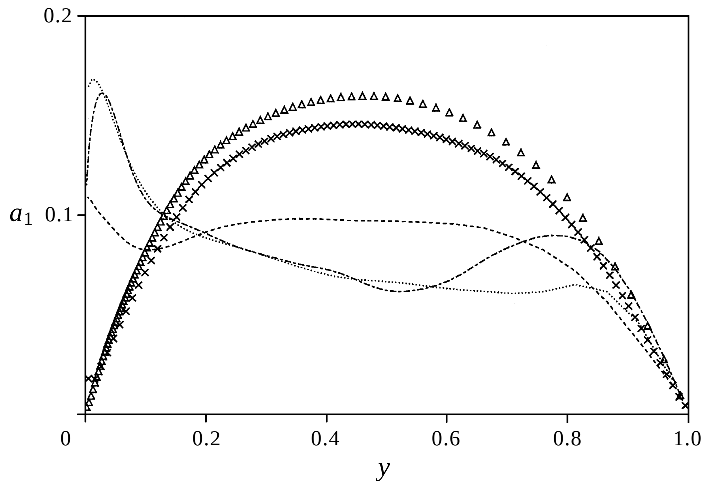

FIGURE 7. Structure parameter profiles: ---- , $N = 0.5$; ········ , $N = 1.0$; —— , $N = 2.0$; △ , $N = 0$; × , EUW.

boundary layer, a_1 increases. In the case of the rotating pipe flow the parameter a_1, defined as $a_1 = [\langle v_r'v_z'\rangle^2+\langle v_r'v_\theta'\rangle^2+\langle v_z'v_\theta'\rangle^2]^{1/2}/\overline{q^2}$, decreases in the centre of the pipe with the increase of the rotation and increases near the wall (figure 7). The increase near the wall is due to the diminishing of turbulent energy and to the increase of $\langle v_\theta'v_z'\rangle$. The value at $N = 0$ at the centre of the pipe is slightly greater than the experimental value $a_1 = 0.14$ found in the zero-pressure-gradient turbulent boundary layer. By comparing the present results with those of three-dimensional boundary layers we could draw the conclusion that the changes of a_1 are ascribed to the sideways tilting of the wall structures by the cross-flow. In the boundary layers this effect is limited to a narrow layer, while in the pipe it extends throughout the whole flow. Only at high rotation speed does the wall region of the pipe show an increase similar to that measured in the outer region of the three-dimensional boundary layer. This fact is related to modifications of the vortical structures by the cross-flow that reduce the production of turbulent energy. These changes in the second-order statistics in a pipe with the rotation rate make it a very challenging case to validate new ideas in Reynolds-averaged turbulent models for complex flows. In particular, this case is very useful for improving turbulence models related to swirling flows, which are very important in the design of combustion chambers.

High-order statistics such as skewness and flatness give a further indication of the intermittent character of the wall region. In the plane channel KMM have shown that the flatness and the skewness of the normal velocity have variations larger than the other two components, thus only the profiles of $\langle v_r'^3\rangle/\langle v_r'^2\rangle^{3/2}$ and $\langle v_r'^4\rangle/\langle v_r'^2\rangle^2$ are presented. In our convention $v_r > 0$ is directed towards the wall; to have the same notation as the plane channel, the quantity $w_r = -v_r$ must be used, so that the usual meaning for the ejection and sweep events is maintained. Figure 8(*a*) shows that the skewness of w_r' has the zero crossing at $y_d \approx 0.25$ for $N = 0$ in very good agreement with the value obtained by EUW in the pipe and with that by KMM in the plane channel. For $N < 1$ the absolute values of the peak near the wall increase with N, but the zero-crossing position does not change appreciably. On the other hand, for $N \geqslant 1$ the position of zero crossing moves towards the wall and a minimum on the profile occurs close to the zero crossing. These large variations of the skewness with the

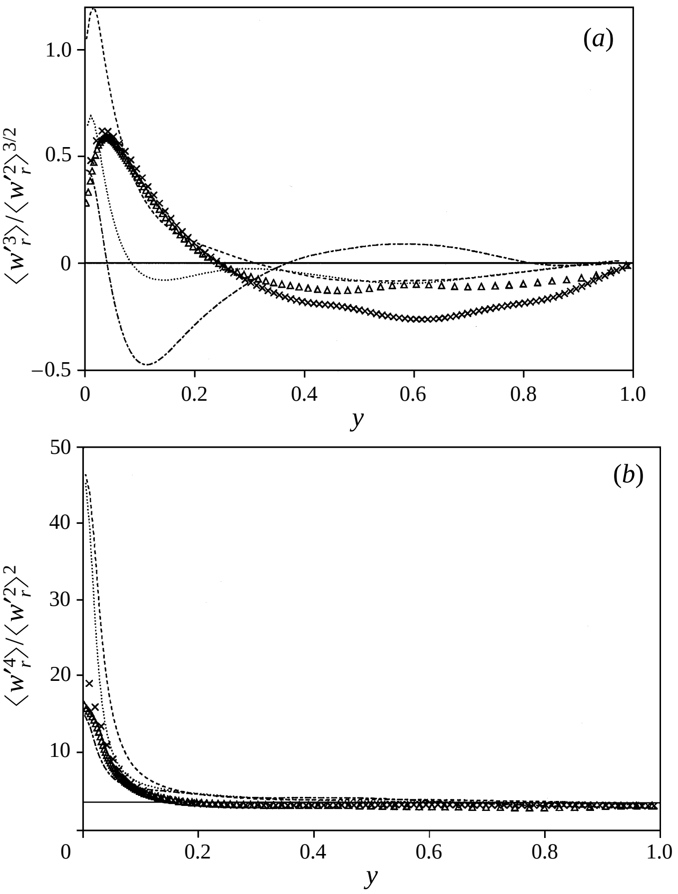

FIGURE 8. Profiles of (*a*) skewness and (*b*) flatness of the radial velocity: ---- , $N = 0.5$; ········ , $N = 1.0$; — - — , $N = 2.0$; △ , $N = 0$; × , EUW.

rotation rate are a further indication that changes of the orientation of the vortical structures occur near the wall, and that the inclination is responsible for the events producing the stresses $\langle v_r'v_\theta'\rangle$ and $\langle v_z'v_\theta'\rangle$.

As in the KMM simulation, in contrast to the experiments, very high values for the flatness of v_r' occur at the wall (figure 8*b*). There are minor differences between the present and the EUW results at $N = 0$, for $y < 0.05$, but in the remaining part of the pipe the agreement is good. When the pipe rotates, very close to the wall the flatness increases up to $N = 1$ and decreases for $N = 2$. The increase of $\langle v'^4\rangle/\langle v'^2\rangle^2$ at $y = 0.2$ is an indication of large regions of low fluctuations and of narrow zones with high fluctuations levels, as contours of ω_r' in the (z, θ)-planes show (figure 10*a*). The flatness of v_z' (not reported in this paper) shows a continuous increase with N, indicating that near the wall the flow becomes more intermittent with the rotation. The more intermittent nature of the wall region at $N = 2$ is displayed by a comparison between contour plots, in z, θ sections at $y_d = 0.079$, of radial vorticity at $N = 0$ (figure 9*a*) and at $N = 2$ (figure 10*a*). When the pipe does not rotate the thin layers of ω_r' represent the high- and low-speed streaks that contribute to the turbulent drag and to the $\langle v_r'v_z'\rangle$ Reynolds stress. The positive values (solid lines in figure 9*a*) indicate the passage from a low- to a high-speed streak. Contour plots, at the same y_d, of v_z' in

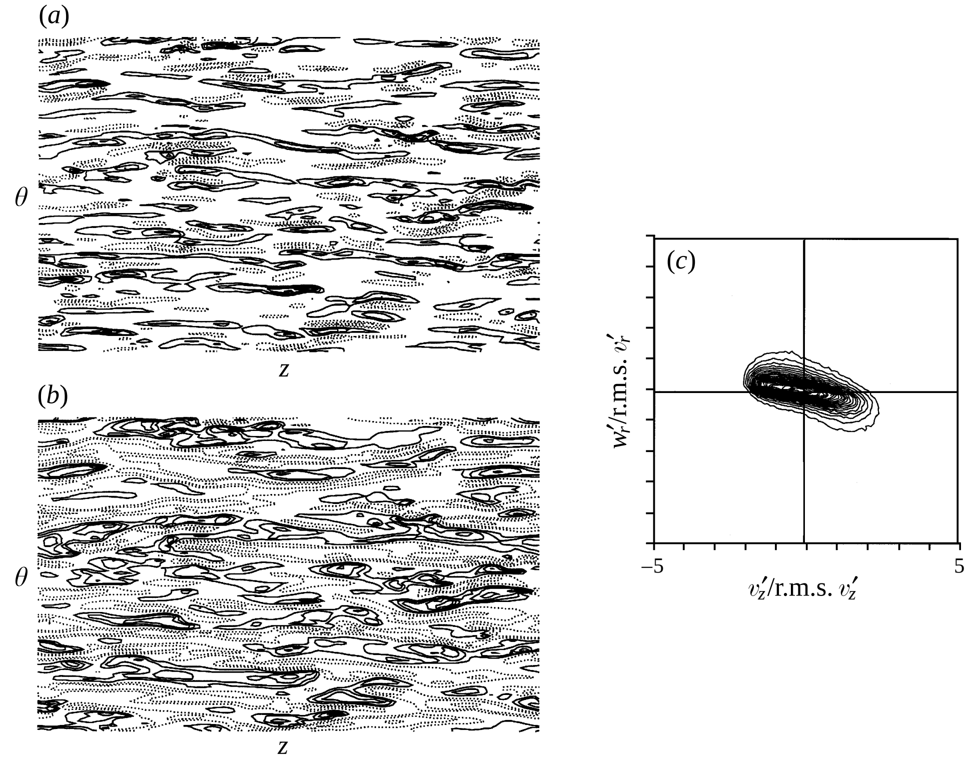

FIGURE 9. Contour plots at $y^+ = 10$ for $N = 0$ of (*a*) ω_r', with $\Delta\omega_r' = 0.75$ (*b*) v_z', with $\Delta v_z' = 0.05$, (*c*) joint p.d.f. of v_z' and $w_r' = -v_r'$ scaled by the local r.m.s. value, contours level $\Delta = 0.0002$.

figure 9(*b*) show that the regions of negative fluctuations are longer than those with positive values. This behaviour was also observed in a plane channel by Sendstadt & Moin (1992). Contours of v_r', not presented here, show that in correspondence with $v_z' > 0$ ($v_z' < 0$) there are more points with $v_r' < 0$ ($v_r' > 0$), than points of fluctuations of equal sign. In the bursting process, these sweep and ejection events lie in the fourth and second quadrants of the joint p.d.f. shown in figure 9(*c*). These are the events contributing mainly to $\langle v_r'v_z' \rangle$. The results for the non-rotating pipe confirm that the near-wall flow in the pipe behaves like the near-wall flow in a plane channel. The joint p.d.f.s for the pipe were not evaluated by EUW and even if these had not differed from those in KMM, we are presenting them because the close comparison with those at $N = 2$ permits a better comprehension of the changes in the bursting process with rotation.

In figure 10(*a–c*) the same quantities as before are given for the simulation at $N = 2$. Figure 10(*a*) shows that the regions of high ω_r' are tilted and reduced in number. The regions of $v_z' < 0$ for $N = 2$ are also longer than those of $v_z' > 0$. The greater spacing between the layers is an indication of wider streaks (figure 10*b*) that together with a weakening of the vorticity levels cause the drag reduction. The joint p.d.f. contours in figure 10(*c*) show that the rotation reduces the number of sweeps and ejections and that the contribution of events with equal sign of fluctuations increases. Since the joint p.d.f.s are evaluated for the fluctuations normalized by the r.m.s. it is clear that the sweeps are associated with a smaller in-rush velocity than that for $N = 0$. This plot explains why $\langle v_r'v_z' \rangle$ is not greatly modified by rotation, as was shown in

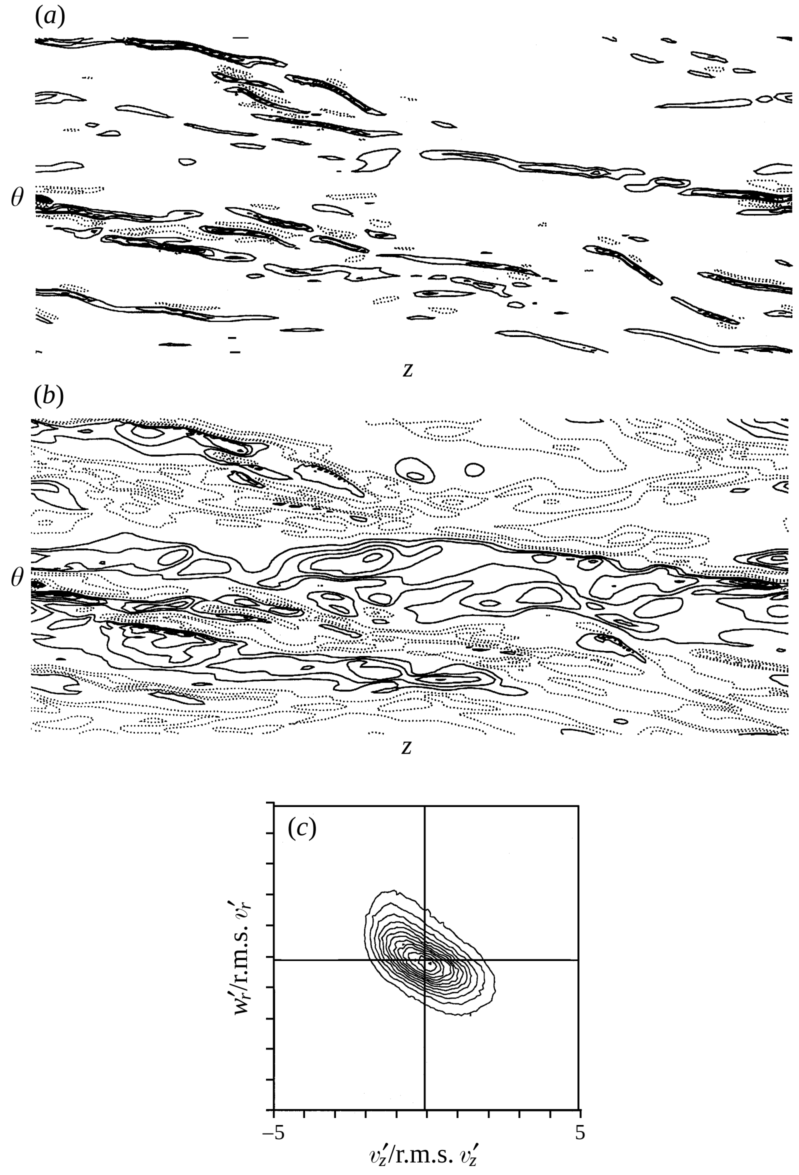

FIGURE 10. Contour plots at $y^+ = 10$ for $N = 2$ of (*a*) ω'_r, with $\Delta\omega'_r = 0.75$ (*b*) v'_z, with $\Delta v'_z = 0.05$, (*c*) joint p.d.f. of v'_z and $w'_r = -v'_r$ scaled by the local r.m.s. value, contours level $\Delta = 0.0002$.

figure 5(*b*). The largest contributions to the negative $\langle w'_r v'_z \rangle$ come from the second (ejections) and fourth (sweeps) quadrants both in the rotating and non-rotating pipe. The reduced number of regions of strong ω'_r indicates a more intermittent flow, as was shown by the flatness profile in figure 8(*b*). The analysis of a single realization of the flow gives a qualitative picture of the streak spacing.

In the rotating and in the non-rotating case the two-point correlations in the stream-wise direction, at $y_d = 0.70$, of the fluctuating velocities give a quantitative measure of the size of the turbulence scales in the central part of the pipe and show whether the simulation is performed in a pipe of sufficient length. The correlations

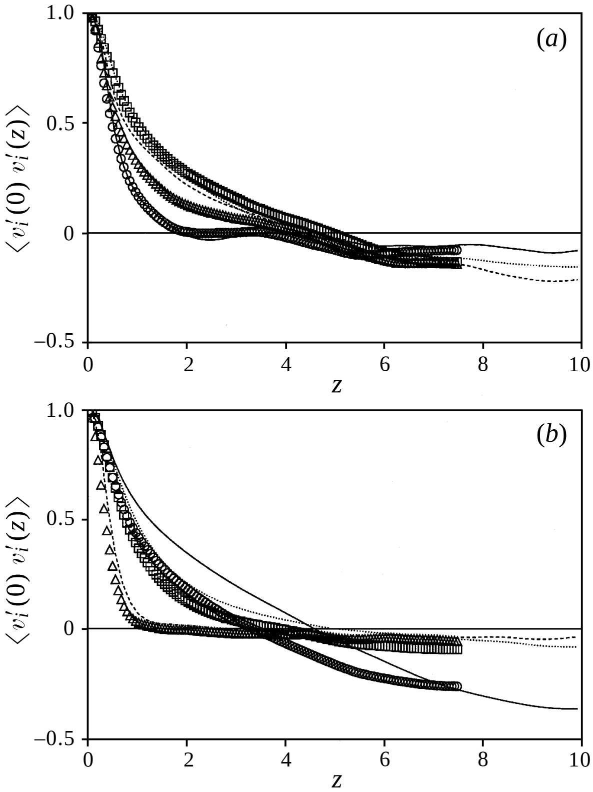

FIGURE 11. Axial two-point correlations for $N = 2.0$: ——— , ○ , $i = \theta$; - - - - , △ , $i = r$; ········ , □ , $i = z$; (*a*) at $y = 0.70$, (*b*) at $y = 0.08$ (symbols $L_z = 15R$, lines $L_z = 20R$).

in the non-rotating case are not presented since these agree with those presented in EUW. To investigate the dependence of the spanwise correlation on the length of the pipe these have been evaluated by a set of fields calculated for $L_z/R = 15$ and for $L_z/R = 20$. The location of the minima at the end of the pipe length in figure 11(*a*) indicates that, at high N, at the centre there are very elongated structures spanning the full pipe. These structures were visualized by Nishibori *et al.* (1987). The two-point correlations explain why no convergence of the statistical quantities to a steady state was found when a length $L_z/R = 10$ was used. In fact this length was not sufficient to let the elongated structure in figure 10(*d*) develop. The two-point correlations near the wall (figure 11*b*), at $N = 2$ and $y_d = 0.08$, show that near the wall the structures are also correlated along the full extent of the pipe in accordance with the visualizations in figure 10(*e*). Figure 11(*b*) furthermore shows that the scales associated with v_r' are the smallest and that the largest are those associated with v_z'.

Two-point velocity correlations in the azimuthal directions furnish quantitative information on the streak spacing. The simulations show that at $N = 2$ these correlations are independent of the length of the pipe, thus these have been plotted for the simulation at $L_z/R = 15$ at $y_d = 0.08$, which approximately corresponds to the distance of maximum turbulent energy production. The correlations for $N = 0$ do not differ from those in the plane channel and are shown in this paper (figure 12*a*) because a direct comparison with those at $N = 2$ permits a better understanding of the modifications of the vortical structures. At $N = 0$ figure 12(*a*) shows that

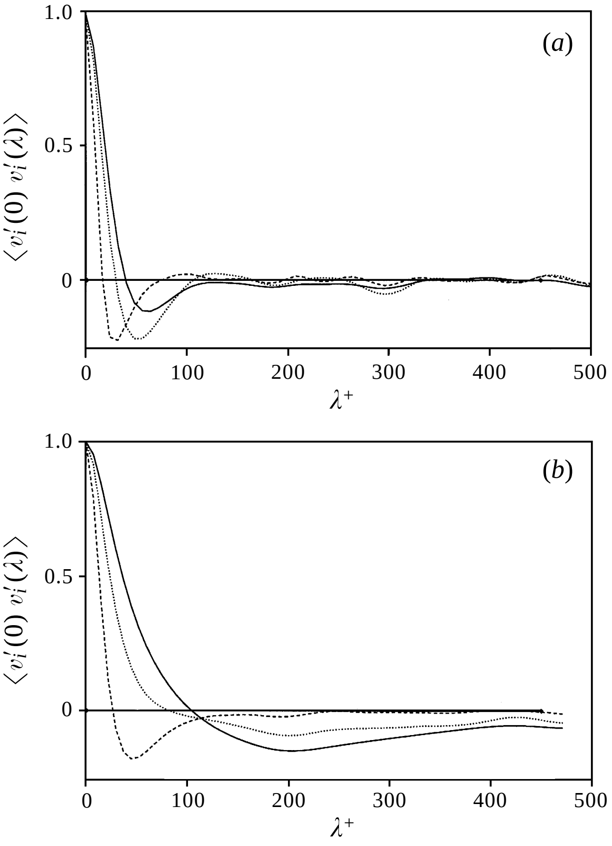

FIGURE 12. Spanwise two-point correlations at $y = 0.078$: ——— , $i = \theta$; - - - - , $i = r$; ········ , $i = z$; (*a*) $N = 0$; (*b*) $N = 2.0$.

the minimum of the correlation of the axial velocity occurs at $\lambda^+ = r^+\theta = 50$, the characteristic streak spacing of 100 wall units. Figure 12(*a*,*b*) shows that from $N = 0$ to $N = 2$ the locations of the minima of the correlation of v_z', v_θ' and v_r' increase by different amounts; this fact indicates that the increase is not related only to the growth of r^+, which depends on the decrease of u_τ. The modifications of the two-point correlations are thus connected to the modifications of the vortical structures in the wall region. From figures 9(*b*), and 10(*e*) (which contain information related to a single realization), and from figures 12(*a*, *b*) (which include a large number of events), it is clearly shown that widening and tilting of the wall streaks occurs in the rotating case.

The tilting of the vortical structures was shown by Sendstad & Moin (1992) in a plane channel with spanwise mean pressure gradient. From these two different simulations we can speculate that when the positive and negative streaks are not aligned with the streamwise velocity, the regeneration process is reduced. In the present case a helical motion lifts the vortical structures away from the wall producing a reduced amount of opposite-sign vorticity at the wall. These thin layers, the precursors of the streamwise vortices, roll up and increase in strength by vortex stretching. This mechanism was clearly described for the plane channel with and without lateral pressure gradient by Sendstad & Moin (1992). We wish to point

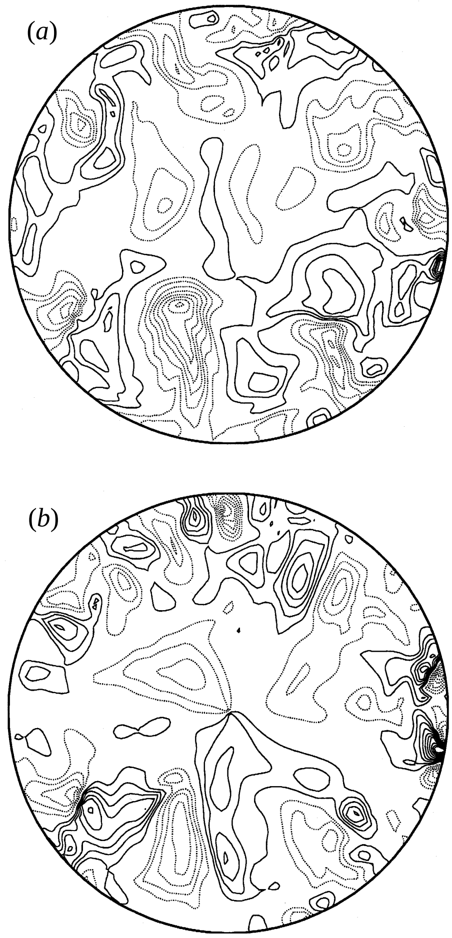

FIGURE 13. Contour plots of (*a*) v_z' and (*b*) v_r' scaled by the r.m.s. value at each r for $N = 0$ in a vertical section; contour level $\Delta = 0.5$.

out that, as in the channel with lateral pressure gradient, in the rotating pipe the mechanism of regeneration remains, but it is largely reduced. These changes on the near-wall vortical structures produce an effect on the distribution of v_z'. Figure 10(*b*), in fact, shows that for $N = 2$, the number of contour levels of v_z' is less than that for $N = 0$ (figure 9*b*), and this explains why in figure 5(*c*) the peak of the r.m.s. of v_z' decreases with N.

In the rotating case the simulations predicted a decrease in the skin friction and in the magnitude of the Reynolds stress; the physical explanation is obtained by comparing, at $N = 0$ and $N = 2$, contour plots on (r, θ)-planes of the same quantities as in the joint p.d.f.s of figure 9(*c*) and figure 10(*c*). These visualizations are a further tool to explain the effects of the rotation on the turbulence profiles shown in figure 5. The contours of v_z' and v_r' shown in figures 13(*a*,*b*) indicate in a different way the same outcome as from the joint p.d.f. in figure 9(*c*): that for $N = 0$, in the region close to the wall, these fluctuations are highly correlated, and that the events producing an in-rush of fluid towards the wall are more intense. In figure 13(*b*) v_r' divided by its r.m.s. is plotted. Positive values represent parcels of fluid moving towards the wall. Since the numerator and the denominator both tend to zero while

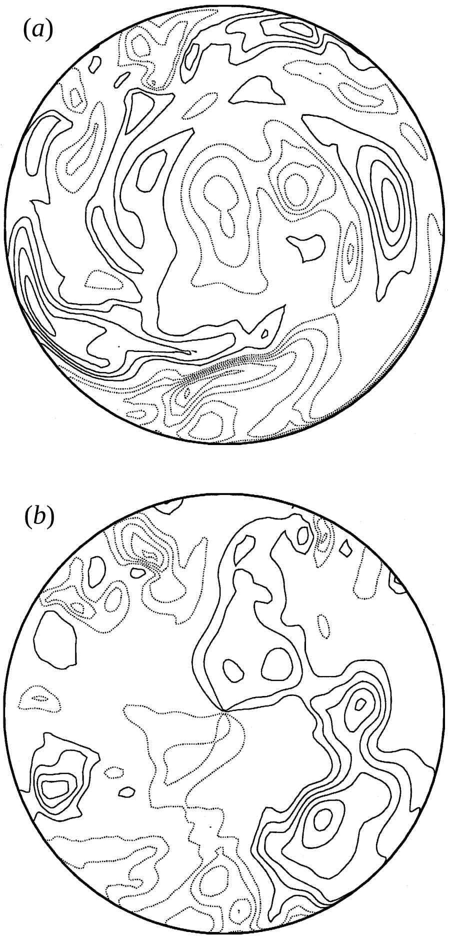

FIGURE 14. Contour plots of (*a*) v_z' and (*b*) v_r' scaled by the r.m.s value at each r for $N = 2$, in a vertical section; contour level $\Delta = 0.5$.

approaching the wall, figure 13(*b*) gives the impression of a free-slip wall. When the pipe rotates, figure 10(*c*) shows that the number of intense sweeps is reduced; in fact the number of locations at $y_d = 0.079$ with high values of $v_r' > 0$ is reduced as the comparison between figure 14(*b*) and 13(*b*) shows. At $N = 2$, these plots could give an erroneous impression that the fluctuations did not increase in the central part of the pipe in contrast to the profiles in figure 5(*b, c*). Contours, not scaled by the local r.m.s., as in figure 5(*b, c*), reveal an increase of the turbulent intensities in the central region. Figure 14(*a*) gives a clear picture that the helical motion is responsible for the transport of the fluctuations from the wall to the central region.

In the non-rotating pipe, the Reynolds stresses $\langle v_\theta' v_z' \rangle$ and $\langle v_\theta' v_r' \rangle$ are zero because of symmetry. This also means that in the joint p.d.f. of v_z' and v_θ' (not reported here) there is a cancellation of the contributions from the first and fourth quadrants. The same cancellations between the second and third quadrants occurs, but the number of events in the first and fourth quadrants, at $y^+ \approx 10$, exceeds the number of events in the other quadrants; the opposite occurs in the central part of the pipe. This difference between the wall and the central part is congruent with the change of sign of the skewness of v_z'. The direct simulations permit us to investigate which events

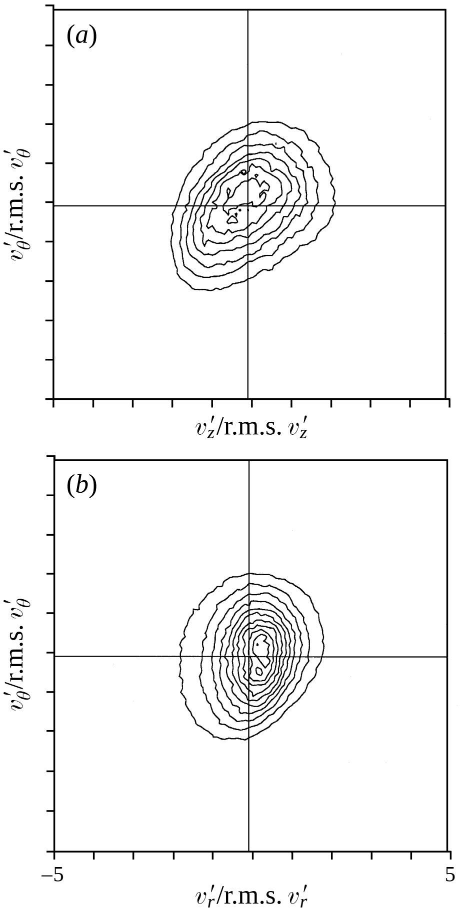

FIGURE 15. Joint p.d.f. of (*a*) $v'_z\ v'_\theta$ and (*b*) $v'_r\ v'_\theta$ scaled by the local r.m.s. for the rotating pipe at $N = 2$; contour level $\Delta = 0.0002$.

contribute to the $\langle v'_\theta v'_z \rangle$ and $\langle v'_\theta v'_r \rangle$ stresses when the symmetry is disrupted by the pipe rotation. At $N = 2$ near the wall (figure 6*a*) the stress $\langle v'_\theta v'_z \rangle$ is greater than $\langle v'_z v'_r \rangle$ (figure 5*d*); this stress is positive, thus the first and third quadrants give the largest contribution. In addition the joint p.d.f. in figure 15(*a*) shows that the events in the third quadrant give a greater contribution than those in the first quadrant. This means that the rotation increases the correlation between low-speed streaks and regions of negative v'_θ. This plot has been evaluated at the same location as that of figure 10(*f*) implying that there is an azimuthal fluctuation in the direction of rotation associated to the in-rush events and vice versa when there is an ejection. This occurrence is also displayed in figure 15(*b*) showing a more isotropic joint p.d.f. Therefore it is clear why $\langle v'_\theta v'_r \rangle$ is smaller (figure 6*b*) than $\langle v'_z v'_r \rangle$ (figure 5*d*). We would like to point out that the sign of $\langle v'_\theta v'_r \rangle$ depends on the direction of the rotation.

Robinson (1991) in an analysis of the turbulent boundary layers of Spalart (1988), and of the plane channel flow of KMM noticed a strong correspondence between low-pressure regions and streamwise vortices. Kim (1989), on the other hand, through the joint p.d.f between pressure and streamwise vorticity, found that peaks of ω'_z are associated with large negative fluctuations of pressure but not vice versa. In the

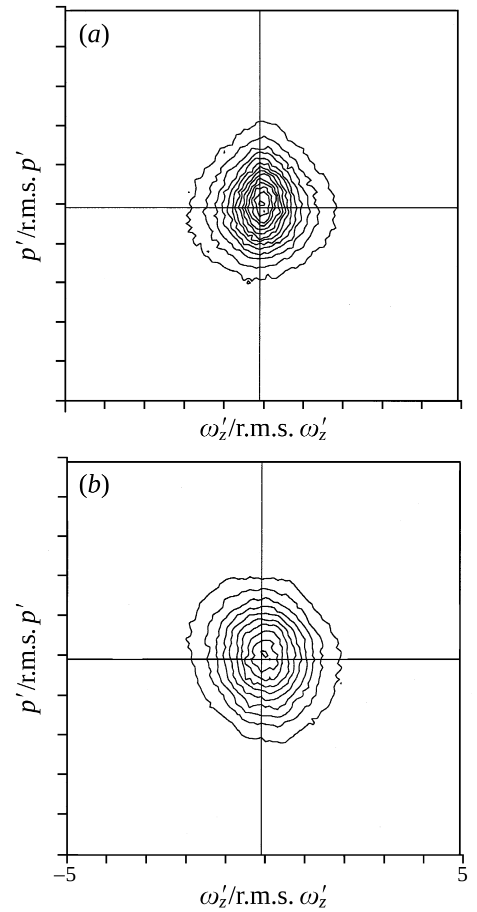

FIGURE 16. Joint p.d.f. of p' and ω'_z at $y = 0.078$ for (*a*) $N = 0$ and (*b*) $N = 2$; contour level $\Delta = 0.0002$.

present simulation at $N = 0$ figure 16(*a*) shows that near the wall what was observed by Kim (1989) is reproduced. We would like to point out that the correlation between p' and ω'_z is better observed in the region far from the wall. In the rotating case the joint p.d.f, in figure 16(*b*), shows that high values of positive pressure are associated with negative streamwise vorticity and vice versa. This change of sign of the extreme values of the pressure with the streamwise vorticity indicates that the shear prevails over the vorticity. The correlation between p' and ω'_z is elucidated in figure 17 and figure 18, by contour plots of these quantities, scaled with the local r.m.s. value, in the same horizontal section as figures 9(*a*, *b*) and 10(*a*, *b*). Moreover, the comparison between visualizations of ω'_z in the rotating and in the non-rotating case shows that the external rotation increases the axial correlation of the streamwise vorticity. In order to study the vorticity dynamics subjected to background rotation, the rotating pipe is very interesting since it is a flow with streamwise vorticity that is generated in the wall layer by vortex stretching and tilting oriented along the rotation axis. Figure 17 shows contour plots of the quantities in figure 16 for $N = 0$ and figure 18 for $N = 2$. In the rotating case the pressure, an indicator of the total vorticity field, highlights structures larger than those in the non-rotating case, that is the pressure shows that the rotation has produced an amalgamation of small structures. This

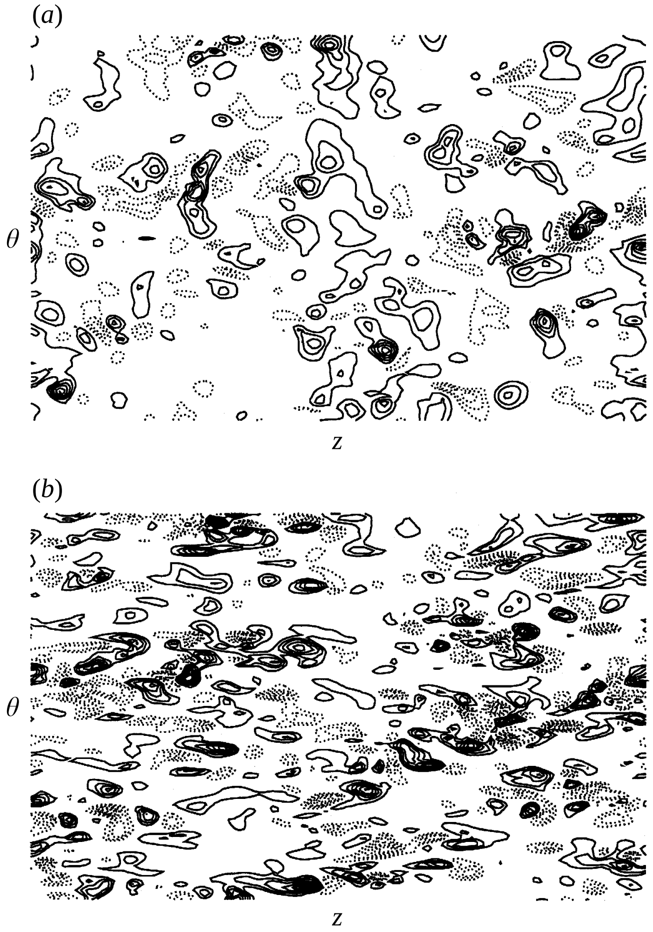

FIGURE 17. Contour plots of (*a*) p' and (*b*) ω'_z scaled by the r.m.s. value at each r for $N = 0$, in a horizontal section at $y^+ = 10$; contour level $\Delta = 0.75$.

amalgamation indicates an inverse energy cascade reminiscent of two-dimensional turbulence. The contour levels of ω'_z for $N = 0$ (figure 17*b*) are closer to each other than for $N = 2$ (figure 18*b*) producing a stronger transport of v'_z towards the wall, thus creating more friction.

4. Conclusions

The present study was devoted to the direct numerical simulation of a turbulent pipe flow with and without rotation. The numerical method was tested in the non-rotating case by comparing the results with the validated simulations by EUW. The grid refinement check showed that using second-order finite differences, even on coarse meshes, turbulence is sustained and the results are reasonable good. This confirms the present tendency to pay a large amount of attention to developing subgrid models for large-eddy simulations by finite differences, a method of wider applicability than spectral models. From these simulations we understood also that there is a strong interaction between numerical and subgrid dissipation, as confirmed by specific studies devoted to this topic such as that by Kravchenko & Moin (1997).

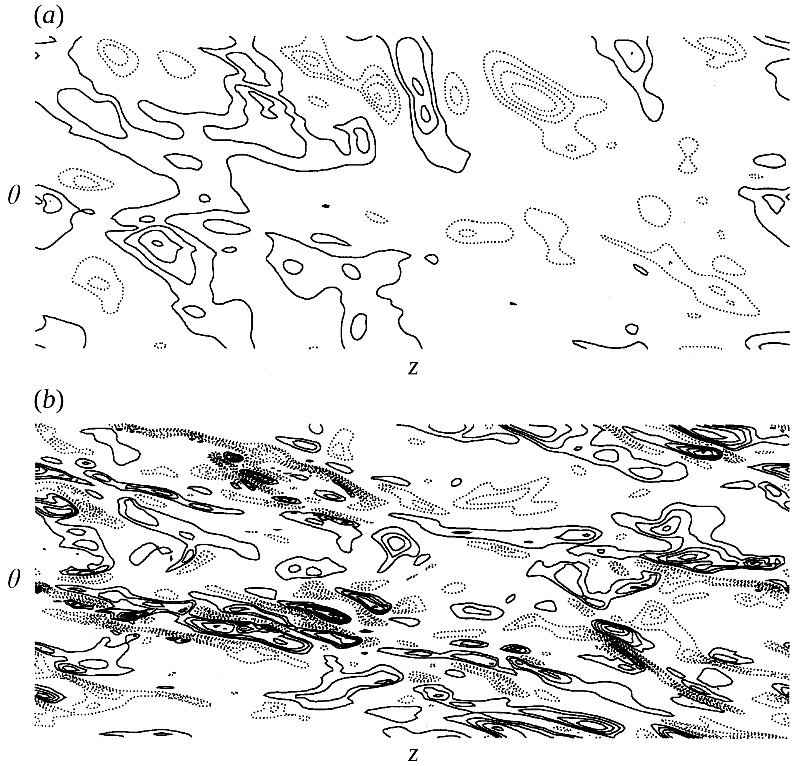

FIGURE 18. Contour plots of (*a*) p' and (*b*) ω_z' scaled by the r.m.s. value at each r for $N = 2$, in a horizontal section at $y^+ = 10$; contour level $\Delta = 0.75$.

The simulations in the rotating case were done in the same range of rotation rates considered in the experiments by Reich & Beer (1989), which are greater than those in the direct simulations by EBN. As in the experiments, it was found that the rotation produces drag reduction and that at high rotation rates the mean streamwise velocity tends to the parabolic laminar Poiseuille profile. From the experiments, Nishibori *et al.* (1987) and Reich & Beer (1989) claimed that the drag reduction and the turbulence suppression was caused by the centrifugal force of the swirling flow component; the present simulations added a further contribution by relating the drag reduction to the modifications of the near-wall vortical structures. A confirmation that the drag reduction is related to the widening of the wall streaks was obtained by two-point velocity correlations in the azimuthal directions. Through flow visualizations of the vorticity field and joint p.d.f.s the changes caused by the rotation on the second- and higher-order statistics were explained. Contour plots of the fluctuating pressure at high rotation have shown the tendency to form large scales with high correlation in the direction of the rotation, in accordance to the Taylor–Proudman theorem. This tendency is characterized by a strong reduction of v_z' and ω_z' and by the large values of contours of pressure fluctuations. The present simulations have the required accuracy in the near-wall region to permit us to draw solid physical conclusions about the mechanism producing the drag reduction. A check of the importance of the computational length in the streamwise direction was done by simulations with constant spatial resolution and different axial length.

Our near-future goal is to apply the present numerical method to LES in the same range of rotation rates and to check whether the dynamic model is appropriate. The hope that this new subgrid model is suitable for rotating flows is based on the satisfactory results recently obtained by Squires & Piomelli (1993) in isotropic turbulence subjected to solid-body rotation. Since the dynamic model gave satisfactory predictions in the plane channel we think that the rotating pipe is a very challenging case to check whether this model could be applied to more complex and realistic situations as those occurring in swirling combustion chambers. Hirai *et al.* (1988), in fact, proved that the conventional k–ϵ turbulence model does not work for the rotating pipe. By the present validated direct simulations, although limited to low Reynolds number, we have created a database which could furnish the Reynolds stress budgets, a useful tool to develop new ideas on one-point closure models.

Finally, the rotating pipe flow is interesting because the rotation is directed in the same direction as the streamwise vorticity. The same amount of positive and negative ω_z is generated at the wall without rotation, while the present simulations show that the solid-body rotation produces a positive mean streamwise vorticity near the wall. This occurrence is related to the longer survival of vorticity of the same sign as that of the external rotation. This aspect of vorticity dynamics in the presence of solid-body rotation was investigated by Bidokhti & Tritton (1992) in a mixing layer where the external rotation is aligned with the main vorticity and normal to the rib vortices. The rotating pipe flow, on the other hand, has the mean vorticity $\langle \omega_\theta \rangle$ orthogonal to the external rotation and the near-wall streamwise vortices, analogous to the rib vortices, aligned with the external rotation, so that it is a case complementary to the mixing layer. The analysis of the differences and the analogies in these two cases could bring a better comprehension of the vorticity dynamics in the presence of background rotation.

This study was initiated while P.O. was visiting the Centre of Turbulence Research. The fruitful discussions with the associated fellows there are appreciated. We wish to thank Dr Eggels who furnished the first draft of his paper on the same topic and the data of the direct simulation of the non-rotating pipe. Particular thanks goes to Ugo Piomelli who carefully criticized the first draft of the paper. The set of coarse simulations was performed on the CRAY YMP2E of the Centro di Supercalcolo di Torino. The most refined simulations were performed on the NASA Ames computers and on the SP2 IBM at CINECA in Casalecchio. On using the SP2 one of us (M.F.) was helped by Dr M. Briscolini of IBM. The support by grants of MURST are also acknowledged. Finally, we give special thanks to two anonymous referees for their useful comments.

Appendix. Accuracy checks

Finite differences permit us in a very simple way to handle free-slip and no-slip boundary conditions and thus to verify whether the non-uniform spacing maintains the energy conservation in the inviscid limit. This check was done by performing a coarse simulation (65×39×33) for $\nu = 0$ and with a free-slip boundary. The calculation was started from a viscous unresolved simulation at $Re = 4900$, corresponding to $Re_\tau \approx 180$, and it was left free to evolve to a statistical steady state. In this case, the mean pressure gradient drops to zero and the mean axial velocity profile tends to be constant across the pipe. Figure 19(*a*) shows that the total energy remains constant and that the total turbulent energy decreases due to the reduction of turbulent energy production caused by the diminishing of the mean shear. Figure 19(*b*), in

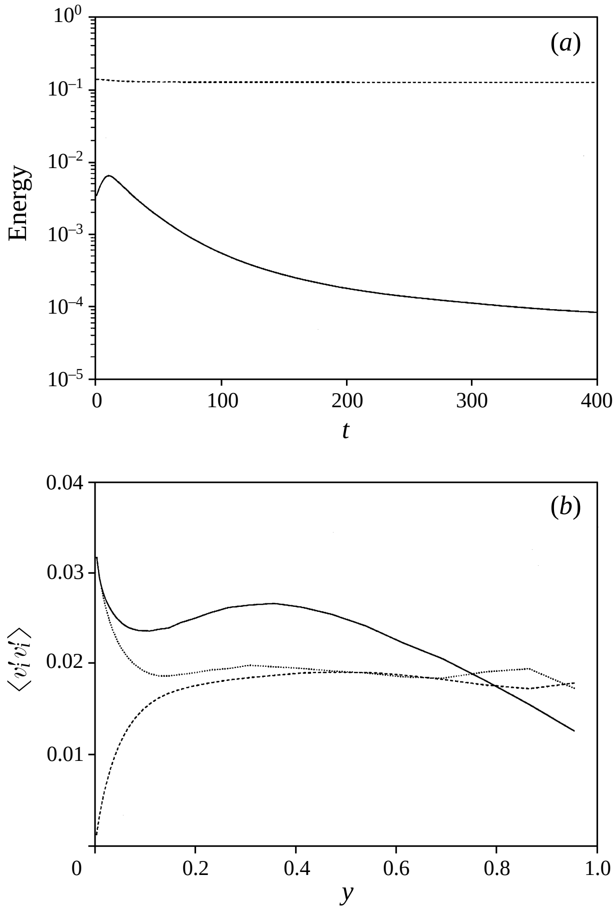

FIGURE 19. (*a*) Time history of total (----) and turbulent (———) energies; (*b*) profiles of the normal stresses ———, $i = z$; ----, $i = r$; ········, $i = \theta$.

addition, shows that the radial profiles of each of the normal turbulent stresses reach the condition of almost isotropic turbulence within a large part of the pipe. The $v_r = 0$ assumption is the cause of the anisotropy near the free-slip wall. This check proves that second-order centred finite differences, for the nonlinear terms, do not introduce any spurious numerical viscosity, which for positive values could lead to unphysical dissipation and for negative values to unphysical production of energy. The influence of aliasing errors on finite-difference methods is not as important as on pseudo-spectral methods. Kravchenko & Moin (1997) have analysed these errors for different schemes for the nonlinear terms and they have shown that aliasing errors are negligible when staggered variables are used. However we wish to recall that truncation and aliasing errors are very important for large-eddy simulations but not for direct numerical simulations, where all the significant scales must be resolved.

A test of the accuracy of the viscous-term discretization and of the entire numerical method was performed by a grid refinement check. In the non-rotating case this check was done starting from a very coarse grid ($32 \times 38 \times 16$) and then doubling the number of points in the θ- and z-directions until reaching the grid $128 \times 96 \times 128$. A non-uniform grid in r with an enhanced clustering near the wall located the first point at

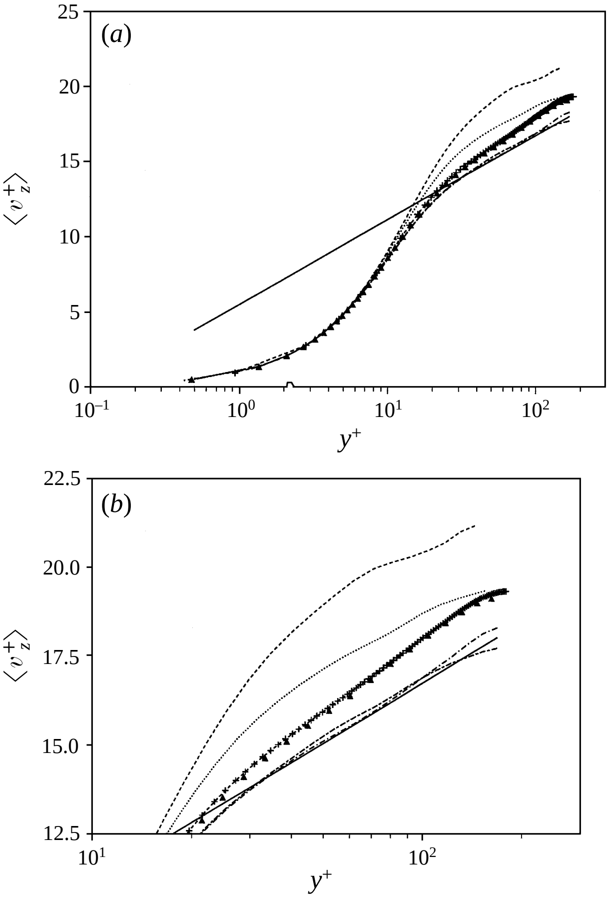

FIGURE 20. Mean axial velocity profiles in wall coordinates: ——— , log law $(1/0.41)\ln y^+ + 5.5$; - - - - , 33 × 39 × 17; ········ , 65 × 39 × 33; —·— , 65 × 39 × 65; — — — , 129 × 39 × 65; ▲, 129 × 49 × 129; +, 129 × 97 × 257; EUW.

$y^+ = 0.5$. The present results are compared with those by EUW, which were validated by comparison with PIV and LDA measurements and with the direct simulation of KMM in a plane channel. For all grids figures 20(*a*, *b*) shows that some sort of logarithmic profile is achieved, but the values of the von Kármán constant depend on the resolution. In figure 20(*a*) the full profile is shown, while in figure 20(*b*) only the part within the buffer and the log regions is shown to emphasize the differences with the log law $\langle v_z^+ \rangle = (1/0.41)\ln y^+ + 5.5$ and with the numerical results by EUW. By $\langle\rangle$ we denote space averages in the two homogeneous directions z and θ and time averages every 10 time steps for a long physical time. The averaging time depends on the case studied: for $N = 0$ the averages were performed for 200 time units, and this time was found to be sufficient. The 128 × 48 × 128 simulation, which uses fewer points than the EUW simulation, is in very good agreement with their results. The good agreement is due to the non-uniform grid, which allows 48 points to be sufficient to locate the first point closer to the wall than the 96 equidistant points in EUW.

From physical arguments changes in the log law should be expected: the decrease of the number of points causes a worse resolution of the near-wall streamwise vortices.

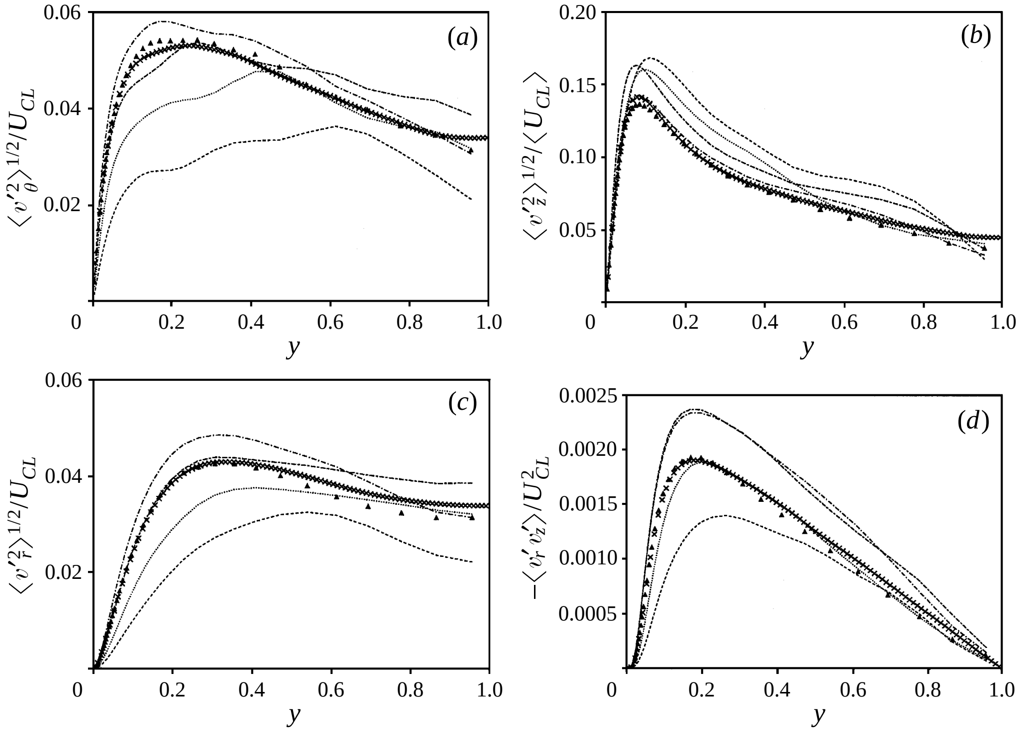

FIGURE 21. Second-order turbulence statistics: - - - - , 33 × 39 × 17; ········ , 65 × 39 × 33; —·— , 65 × 39 × 65; — — — , 129 × 39 × 65; ▲, 129 × 49 × 129; ×, 129 × 97 × 257 EUW.

Since these vortices are responsible for the turbulent wall friction, a decrease in their strength produces a drag reduction. This effect is reflected in figure 21 by the r.m.s. profiles, showing a decrease of the v_r and v_θ r.m.s., and an increase of the v_z r.m.s. The increase of the fluctuations in the streamwise direction is due to a reduction on the mean velocity centreline. Figure 21(*a–d*) shows that the refinement in θ has a greater influence than that in z. The physical reason is that the better resolution of the azimuthal gradients of ω_z gives a better rendering of the sweep and ejection events and hence greater values of $\langle\omega_\theta\rangle$. The observation that streamwise vorticity produces the high- and low-speed streaks, and thus the turbulent wall friction, was made by KMM based on observations made in a plane channel direct simulation, and was also proved by Orlandi & Jimenez (1994) by a two-dimensional model. The results in figure 21 show that the refinement in the axial direction is less important; in fact, the profiles using 128 × 48 × 64 and using 128 × 48 × 128 points do not differ largely from those by EUW using 128 × 96 × 256 points. In figure 21(*d*) the Reynolds stress profiles of $\langle v_r' v_z'\rangle$ confirm that the coarsest simulation gives a sort of drag reduction. The reduction of $\langle v_r' v_z'\rangle$ is mainly due to a decrease of v_r', as in all situations in which a drag reduction is achieved.

For the rotating case the check of the numerics was performed only at $N = 2$. In the rotating case the check must be done not only on the resolution but also on the length of the computational domain in the streamwise direction. In fact, if the pipe was too short it could affect the long helical structures near the wall and at the centre of pipe. The near-wall structures are smaller than those at the centre and have shorter time scales. The statistical steady state is obtained by averaging a few

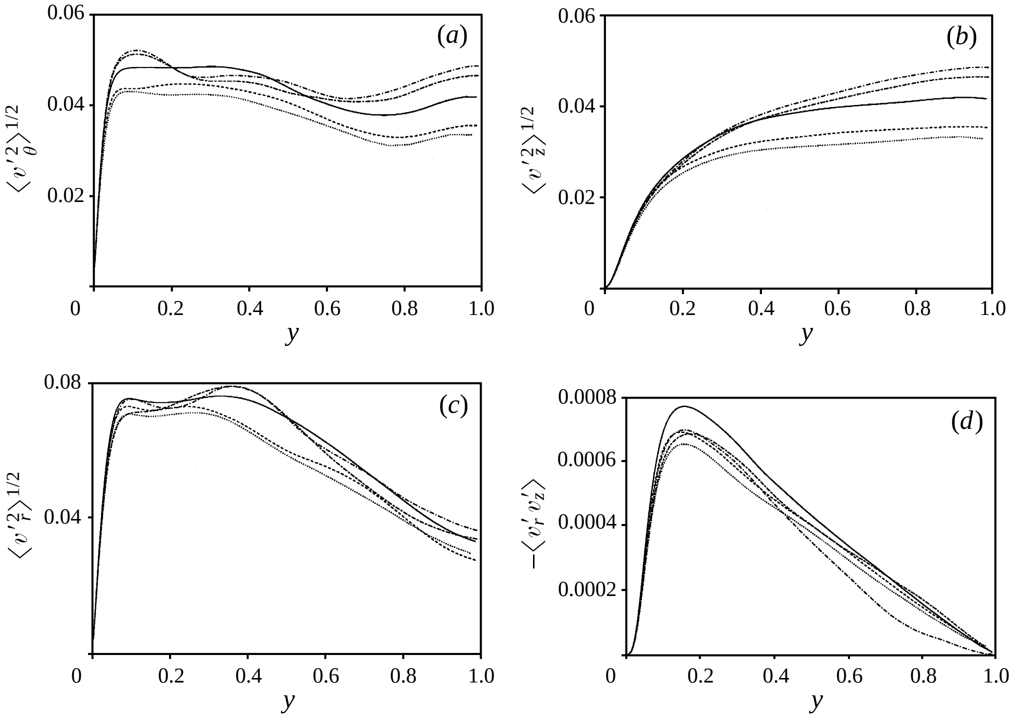

FIGURE 22. Second-order turbulence statistics: ---- , 129 × 49 × 129, $L_z = 10R$; ······· , 129 × 97 × 129, $L_z = 10R$; — — — , 129 × 129 × 129, $L_z = 20R$; —·— , 257 × 129 × 129, $L_z = 20R$; —— , 257 × 97 × 129, $L_z = 15R$.

realizations of the flow near the wall, while it is necessary to average over a larger number of realizations to have satisfactory profiles in the central part. From these arguments it should be expected that the grid resolution and the pipe length should affect more the central than the wall region. We performed simulations on a pipe of length $L_z = 10R$ using grids 128 × 48 × 128 and 128 × 96 × 128 to check the radial resolution. Since a non-uniform grid was used this check is not so important, as was shown for $N = 0$. Two further simulations with $L_z = 20R$ using 128 × 128 × 128 and 128 × 128 × 256 points were performed to investigate the effects of the length and the grid resolution in the streamwise direction. From these simulations it was decided to use the simulation at $N = 2$ with a grid 128 × 96 × 257 in a pipe of length $L_z = 15R$ to analyse the results. With $L_z = 15R$ and with 257 points in z, the resolution in wall units is $\Delta z^+ = 9.5$, small enough to consider the present simulation as a fully direct numerical simulation even in the central region. Figure 22(*a*–*d*) shows that when the pipe is rotating the length of the pipe is an important parameter in the direct simulations.

The final comment on the grid refinement checks is that very coarse calculations in three dimensions give acceptable results that reproduce some of the aspects of wall turbulent flows without introducing any subgrid scale (s.g.s) model. Although a very coarse simulation without an s.g.s. model could be more or less useful, from a physical point of view accurate LES simulations are always better. However, since this numerical viscosity produces energy spectra decreasing reasonably well at high wavenumbers, it is possible that these truncation errors affect the flow in the same manner as s.g.s. models do.

REFERENCES

Bidokhti, A. A. & Tritton, D. J. 1992 The structure of a turbulent free shear layer in a rotating fluid. *J. Fluid Mech.* **241**, 469–502.

Durbin, P. A. 1991 Near-wall turbulence closure modeling without "damping functions". *Theor. Comput. Fluid Dyn.* **3**, 1–13.

Eggels, J. G. M., Boersma, B. J.& Nieuwstadt, F. T. M. 1994*a* Direct and large eddy simulations of turbulent flow in an axially rotating pipe. Preprint (referred to herein as EBN).

Eggels, J. G. M., Unger, F., Weiss, M. H., Westerweel, J., Adrian, R. J., Friedrich, R. & Nieuwstadt, F. T. M. 1994*b* Fully developed turbulent pipe flow: a comparison between direct numerical simulation and experiment. *J. Fluid Mech.* **268**, 175–209 (referred to herein as EUW).

Hirai, S., Takagi, T. & Matsumoto, M. 1988 Prediction of the laminarization phenomena in an axially rotating pipe flow. *Trans. ASME J. Fluids Engng* **110**, 424–430.

Kikuyama, K., Murakami, M. & Nishibori, K. 1983*a* Development of three dimensional turbulent boundary layer in an axially rotating pipe. *Trans. ASME J. Fluids Engng*. **105**, 154–160.

Kikuyama, K., Murakami, M. & Nishibori K. & Maeda, K. 1983*b* Flow in an axially rotating pipe (a calculation of flow in the saturated region). *Bull. JSME* **26**, 506–513.

Kim, J. 1989 On the structure of pressure fluctuations in simulated turbulent channel flow. *J. Fluid Mech.* **205**, 421–451.

Kim, J., Moin, P. & Moser, R. 1987 Turbulence statistics in fully developed channel flow at low Reynolds number *J. Fluid Mech.* **177**, 133–166 (referred to herein as KMM).

Kravchenko, A. G. & Moin, P. 1997 On the effect of numerical errors in large eddy simulations of turbulent flows. *J. Comput. Phys.* **313**, 310–322.

Laufer, J. 1954 The structure of turbulence in fully developed pipe flow. *NACA Rep.* 1174.

Loulou, P. 1996 Direct simulation of incompressible pipe flow using a B-spline spectral method. Thesis Department of Aeronautics and Astronautics, SUDAAR 683, Stanford University.

Murakami, M. & Kikuyama, K. 1980 Turbulent flow in axially rotating pipes. *Trans. ASME J. Fluids Engng* **102**, 97–103.

Nishibori, K., Kikuyama, K. & Murakami, M. 1987 Laminarization of turbulent flow in the inlet region of an axially rotating pipe. *JSME Intl J.* **30**, 255–262.

Orlandi, P. & Jiménez, J. 1994 On the generation of turbulent wall friction. *Phys. Fluids* **6**, 634–641.

Rai, M. M. & Moin, P. 1991 Direct simulations of turbulent flow using finite-difference schemes. *J. Comput. Phys.* **96**, 15–53.

Reich, G. & Beer, H. 1989 Fluid flow and heat transfer in axially rotating pipe 1. Effect of rotation on turbulent pipe flow. *Intl J. Heat Mass Transfer* **32**, 551–561.

Reynolds, O. 1883 An experimental investigation of the circumstances which determine whether the motion of water shall be direct or sinuous, and the law of resistance in parallel channels. *Phil. Trans. R. Soc. Lond.* **174**, 935.

Robinson, S. K. 1991 Coherent motions in the turbulent boundary layer. *Ann. Rev. Fluid Mech.* **23**, 601–639.

Schwarz, W. R. & Bradshaw, P. 1994 Turbulence structural changes for a three-dimensional boundary layer in a 30° bend. *J. Fluid Mech.* **272**, 183–209.

Sendstad, O. & Moin, P. 1992 The near wall mechanics of three-dimensional turbulent boundary layers. Rep. TF-57, Thermosciences division, Department of Mechanical Engineering Stanford University.

Spalart, P. R. 1988 Direct simulation of turbulent boundary layers up to $Re_\theta = 1410$. *J. Fluid Mech.* **187**, 61–98.

Squires, K. D. & Piomelli, U. 1993 Large-eddy simulation of rotating turbulence using the dynamic model. *9th Symp. on turbulent shear flows, Kyoto 17-3.*

Verzicco, R. & Orlandi, P. 1996 A finite difference scheme for direct simulation in cylindrical coordinates. *J. Comput. Phys.* **123**, 402–413.

Zeman, O. 1995 The persistence of trailing vortices – a modeling study. *Phys. Fluids* **7**, 135–143.

Zhang, Y., Ghandi, A., Tomboulides, A. G., & Orszag, S. A. 1994 Simulation of pipe flow. *Applications of Direct and Large Eddy Simulations to transition and turbulence. AGARD Conf. Proc.* 551 17-1–9.